

# Accelerating core-level $GW$ calculations by combining the contour deformation approach with the analytic continuation of $W$ .

Ramón L. Panadés-Barrueta\* and Dorothea Golze\*

*Faculty of Chemistry and Food Chemistry, Technische Universität Dresden, 01062 Dresden, Germany*

E-mail: ramon.lorenzo.panades-barrueta@tu-dresden.de; dorothea.golze@tu-dresden.de

## Abstract

In recent years, the  $GW$  method has emerged as a reliable tool for computing core-level binding energies. The contour deformation (CD) technique has been established as an efficient, scalable, and numerically stable approach to compute the  $GW$  self-energy for deep core excitations. However, core-level  $GW$  calculations with CD face the challenge of higher scaling with respect to system size  $N$  compared to the conventional quartic scaling in valence state algorithms. In this work, we present the CD-WAC method (CD with  $W$  Analytic Continuation), which reduces the scaling of CD applied to the inner shells from  $O(N^5)$  to  $O(N^4)$  by employing an analytic continuation of the screened Coulomb interaction  $W$ . Our proposed method retains the numerical accuracy of CD for the computationally challenging deep core case, yielding mean absolute errors  $< 5$  meV for well-established benchmark sets, such as CORE65, for single-shot  $GW$  calculations. More extensive testing for different  $GW$  flavors prove the reliability of the method. We have confirmed the theoretical scaling by performing scaling experiments on large acene chains and amorphous carbon clusters, achieving speedups of up to 10x for structures of only 116 atoms. This improvement in computational efficiency paves the way for more accurate and efficient core-level  $GW$  calculations on larger and more complex systems.

## 1 Introduction

Core level spectroscopy, particularly X-ray Photoelectron Spectroscopy (XPS), is a powerful analytical technique, which probes the binding energies of the core electrons. XPS provides valuable insights into the elemental composition of the material or molecule and into the chemical environment of the core-excited atom.<sup>1,2</sup> However, the interpretation of XPS spectra is often challenging due to the lack of reference data, necessitating the use of theoretical calculations.<sup>3</sup>

Methods based on density functional theory (DFT),<sup>4,5</sup> specifically the Delta self-consistent field ( $\Delta$ SCF) method,<sup>6</sup> have been widely used for computing XPS spectra.<sup>7–20</sup> While DFT is computationally efficient, it is a ground-state theory and does not provide systematic access to electronic excitations. Problems of  $\Delta$ SCF related to the inclusion of periodicity, constraining the core hole and self-interaction errors have been discussed elsewhere.<sup>21–25</sup>

Rigorous theoretical frameworks for exciting electrons are provided by response methods, where electron propagators are applied to transform the ground to an excited state. In the realm of wave-function-based methods, this includes equation-of-motion coupled cluster (EOM-CC)<sup>26</sup> and the algebraic diagrammatic construction (ADC) scheme.<sup>27,28</sup> Recently, both EOM-CC<sup>29–32</sup> and ADC<sup>31,33</sup> were successfully applied to deep core excitations. An alternative approach is the  $GW$  family of methods,<sup>34–37</sup> which are generally computationally less expensive than wave-function based approaches.<sup>38,39</sup> The fundamental object of the  $GW$  approximation is the one-particle Green's function or electron propagator ( $G$ ), whose imaginary part gives access to the intrinsic spectral function.<sup>37</sup> The latter observable can be directly related to the photocurrent measured in photoemission experiments.

$GW$  has become the method of choice for the calculation of direct and indirect photoemission spectra of solids<sup>37,40</sup> and molecules.<sup>37,41–43</sup> However, the calculation of deep core-level binding energies ( $> 100$  eV) is a very recent trend in

the  $GW$  community.<sup>22,24,44–56</sup> Lately,  $GW$  has also been employed to compute  $K$ -edge transition energies measured in X-ray absorption spectroscopy (XAS) by extension to the Bethe-Salpeter equation (BSE@ $GW$ ).<sup>57</sup> The recent interest in  $GW$  for XPS and XAS computations is driven by its availability in all-electron localized basis set codes, which is a development of the last decade.<sup>37</sup>

$GW$  calculations of core levels are more demanding than their valence counterparts. While an all-electron treatment is the basic requirement for core-level  $GW$ , the following measures must be taken to obtain reliable results and quantitative agreement with experiment: i) We found that highly exact frequency integration techniques for the calculation of the self-energy are necessary, such as a fully analytic treatment or the contour deformation approach.<sup>22</sup> Unlike for valence states, the self-energy has complicated features with many poles. Popular valence-state algorithms using an analytic continuation (AC) of the self-energy fail here drastically. ii) Standard  $G_0W_0$  approach using generalized gradient approximations (GGAs) as starting point suffer from an extreme, erroneous transfer of spectral weight to the satellite spectrum.<sup>47</sup> A distinct quasiparticle (QP) solution is *not* obtained at the  $G_0W_0$ @GGA level. We showed that the inclusion of partial eigenvalue-selfconsistency in  $G$  (ev $GW_0$ ) restores the QP peak. We proposed as computationally cheaper alternatives to ev $GW_0$  either  $G_0W_0$  starting from a hybrid functional with 45% of exact exchange<sup>47,54</sup> or a so-called Hedin shift in  $G$ ,<sup>54</sup> which can be considered a simplified version of ev $GW_0$ . iii) Relativistic effects have also been found to play a major in the correct description of core-level excitations.<sup>48</sup> All three points combined,  $GW$  yields excellent agreement with experiment, with errors  $< 0.2$  eV for absolute and relative binding energies of molecules, respectively.<sup>54</sup> Moreover, we showed for disordered carbon-based materials that we can resolve spectral features within 0.1 eV of the reference experimental spectra when including the  $GW$  correction in the XPS predictions.<sup>24</sup>

The numerical requirements described in i) increase the computational demands compared to valence calculations. A fully analytic evaluation of the self-energy scales  $O(N^6)$  with respect to system size  $N$ .<sup>58</sup> The complexity of core-level  $GW$  calculations with CD, denoted as CD- $GW$  in the following, is with  $O(N^5)$  lower and the reason why we preferred CD over a fully analytic approach previously.<sup>22</sup> However, this is still higher than in canonical  $GW$  implementations with  $O(N^4)$  scaling.<sup>50,58–67</sup> Currently, the  $O(N^5)$  scaling of CD- $GW$  limits its application to systems of  $\approx 100$ –120 atoms. Scaling reduction is thus inevitable in order to address larger system sizes.

The development of low-scaling formulations of  $GW$  is an active field of research. The most popular low-scaling approach is the space-time method<sup>68</sup> which yields cubic scaling algorithms and has gained widespread adoption,

as evidenced by a variety of implementations in, e.g., a plane-wave/projector-augmented-wave  $GW$  code<sup>69</sup> or with localized basis sets using Gaussian<sup>70–72</sup> or Slater-type orbitals.<sup>73–75</sup> However, the space-time method relies on a formulation in imaginary frequency and time, whereas we have a dependency on real frequencies in the CD approach. A direct application of the space-time method is thus not straightforward.

One possible way of reducing the CD scaling is recasting expensive tensor contractions into a linear system of equations that can be solved using, for example, Krylov subspace methods.<sup>76</sup> This approach is used in Ref. 51, which uses the minimal residual method (MINRES) algorithm for the aforementioned purpose, effectively achieving a scaling reduction to  $O(N^4)$ . Despite its potential, this method comes with two significant drawbacks. Firstly, the solver often requires a substantial number of iterations to attain a desirable level of accuracy. Secondly, due to the intricate structure of the self-energy typically observed in core-level states,<sup>22</sup> the method is sensitive to finding solutions which might have a low spectral weight.<sup>51</sup>

In this work, we present a more streamlined and elegant approach to the scaling reduction of CD- $GW$  based on the AC of the screened Coulomb interaction  $W$ , which we denote as CD-WAC (CD with  $W$  analytic continuation). While the AC of the self-energy is very common and implemented in many  $GW$  codes,<sup>60,62,65,66,69–71,73,74</sup> the computational benefits of an AC of  $W$  have hardly been investigated. We are only aware of two references where the latter was used.<sup>49,77</sup> Friedrich *et al.*<sup>77</sup> introduced the idea in the context of the  $T$ -matrix approach.<sup>78</sup> Duchemin and Blase<sup>49</sup> explored the CD-WAC idea for valence states, but provided only a preliminary case study for the O1s excitation of a single  $H_2O$  molecule. Here we advance the CD-WAC approach for deep core-level calculations and show that we can elegantly use it to reduce the scaling of CD- $GW$ .

The paper is structured as follows: in Section 2, we provide an overview of the  $GW$  theory, with strong emphasis on the CD formalism. We then introduce the CD-WAC approach and discuss the choice of the algorithm used for the AC of  $W$ . The Section 3 offers details of the implementation, including a detailed algorithm description. The computational details are presented in Section 4. We then show the results of the accuracy and computational performance benchmarks in section 5. Finally, we provide our conclusions and future perspectives of this work in Section 6.

## 2 Theory

### 2.1 The $G_0W_0$ approximation

The  $GW$  approximation to many-body perturbation theory (MBPT) is derived from the Hedin's equations<sup>37,79</sup> by omit-

ting the vertex corrections. The most important object in  $GW$  is the self-energy, which accounts for exchange and correlation contributions beyond the Hartree-Fock approximation and is given by

$$\Sigma(\mathbf{r}_1, \mathbf{r}_2, \omega) = \frac{i}{2\pi} \int G(\mathbf{r}_1, \mathbf{r}_2, \omega + \omega') W(\mathbf{r}_1, \mathbf{r}_2, \omega') e^{i\omega' \eta} d\omega' \quad (1)$$

where  $G$  and  $W$  are the Green's function and screened Coulomb interaction respectively.

The lowest rung in the hierarchy of  $GW$  approximations is the so-called  $G_0W_0$  approach. The approach perturbatively improves the self-energy corresponding to a mean-field Green's function  $G_0$  by performing a single iteration of the simplified Hedin's equations.<sup>37</sup> A common choice to build  $G_0$  is to use the eigendecomposition of an initial DFT Hamiltonian. In the Lehmann representation<sup>80,81</sup> this can be done as follows:

$$G_0^\sigma(\mathbf{r}_1, \mathbf{r}_2, \omega) = \sum_m \frac{\Psi_{m\sigma}(\mathbf{r}_1)\Psi_{m\sigma}^*(\mathbf{r}_2)}{\omega - \epsilon_{m\sigma} - i\eta \operatorname{sgn}(\epsilon_F - \epsilon_{m\sigma})} \quad (2)$$

where  $\epsilon_{m\sigma}$  and  $\Psi_{m\sigma}$  are the Kohn-Sham (KS) eigenvalues and eigenvectors for the spin channel  $\sigma$ , and  $\epsilon_F$  is the Fermi level. The non-interacting screened Coulomb interaction  $W_0$  is computed in the random phase approximation (RPA):

$$W_0(\mathbf{r}_1, \mathbf{r}_2, \omega) = \int \varepsilon^{-1}(\mathbf{r}_1, \mathbf{r}_3, \omega) v(\mathbf{r}_3, \mathbf{r}_2) d\mathbf{r}_3 \quad (3)$$

where  $v$  is the bare Coulomb interaction, and  $\varepsilon^{-1}$  is the inverse of the dielectric function, which can be computed as:

$$\varepsilon(\mathbf{r}_1, \mathbf{r}_2, \omega) = \delta(\mathbf{r}_1, \mathbf{r}_2) - \int v(\mathbf{r}_1, \mathbf{r}_3) \chi_0(\mathbf{r}_3, \mathbf{r}_2, \omega) d\mathbf{r}_3 \quad (4)$$

In the previous equation we have introduced the irreducible polarizability  $\chi_0$ , which is in practice computed using the Adler-Wisser expression:<sup>82,83</sup>

$$\begin{aligned} \chi_0(\mathbf{r}_1, \mathbf{r}_2, \omega) = & \\ & \sum_\sigma \sum_i^{\text{occ}} \sum_a^{\text{virt}} \left\{ \frac{\Psi_{i\sigma}^*(\mathbf{r}_1)\Psi_{a\sigma}(\mathbf{r}_1)\Psi_{a\sigma}^*(\mathbf{r}_2)\Psi_{i\sigma}(\mathbf{r}_2)}{\omega - (\epsilon_{a\sigma} - \epsilon_{i\sigma}) + i\eta} \right. \\ & \left. - \frac{\Psi_{i\sigma}(\mathbf{r}_1)\Psi_{a\sigma}^*(\mathbf{r}_1)\Psi_{a\sigma}(\mathbf{r}_2)\Psi_{i\sigma}^*(\mathbf{r}_2)}{\omega + (\epsilon_{a\sigma} - \epsilon_{i\sigma}) - i\eta} \right\} \end{aligned} \quad (5)$$

where the indexes  $i, a$  run over occupied and virtual states, respectively.

For computational reasons as well as for better physical interpretation<sup>37</sup> the self energy is usually split into a correlation ( $c$ ) and exchange ( $x$ ) contribution  $\Sigma^\sigma = \Sigma^{c,\sigma} + \Sigma^{x,\sigma}$ . The latter can be expressed in terms of the bare Coulomb

interaction:

$$\Sigma^{x,\sigma}(\mathbf{r}_1, \mathbf{r}_2, \omega) = - \sum_i^{\text{occ}} \Psi_{i\sigma}(\mathbf{r}_1)\Psi_{i\sigma}^*(\mathbf{r}_2)v(\mathbf{r}_1, \mathbf{r}_2) \quad (6)$$

The expression for  $\Sigma^{c,\sigma}$  is analogous to that of Equation (1), but using only the correlation part  $W_0^c$  of the screened Coulomb interaction:

$$W_0^c(\mathbf{r}_1, \mathbf{r}_2, \omega) = W_0(\mathbf{r}_1, \mathbf{r}_2, \omega) - v(\mathbf{r}_1, \mathbf{r}_2) \quad (7)$$

The  $G_0W_0$  QP energy  $\epsilon_{n\sigma}^{G_0W_0}$  for state  $n$  can be computed as first order corrections of the KS eigenvalue  $\epsilon_n$  by solving the following fixed-point equation:

$$\epsilon_{n\sigma}^{G_0W_0} = \epsilon_{n\sigma} + \Re \Sigma_n^\sigma(\epsilon_{n\sigma}^{G_0W_0}) - v_n^{xc,\sigma} \quad (8)$$

where  $v^{xc,\sigma}$  is the exchange-correlation potential from KS-DFT and where

$$\begin{aligned} v_n^{xc,\sigma} &= \int \Psi_{n\sigma}^*(\mathbf{r}_1) v^{xc,\sigma}(\mathbf{r}_1) \Psi_{n\sigma}(\mathbf{r}_1) d\mathbf{r}_1 \\ \Sigma_n^\sigma(\omega) &= \int \Psi_{n\sigma}^*(\mathbf{r}_1) \Sigma^\sigma(\mathbf{r}_1, \mathbf{r}_2, \omega) \Psi_{n\sigma}(\mathbf{r}_2) d\mathbf{r}_1 d\mathbf{r}_2 \end{aligned} \quad (9)$$

In the following, we will omit the explicit spin dependency in order to declutter the notation.

One of the biggest challenges in  $GW$  calculations is the computation of  $\Sigma^c(\mathbf{r}_1, \mathbf{r}_2, \omega)$ . The integral in Equation (1) can be solved analytically (for the correlation part) by computing

$$\Sigma_n^c(\omega) = \sum_m \sum_s \frac{\langle \Psi_n \Psi_m | P_s | \Psi_m \Psi_n \rangle}{\omega - \epsilon_m + (\Omega_s - i\eta) \operatorname{sgn}(\epsilon_F - \epsilon_m)} \quad (10)$$

where  $\Omega_s$  are charge neutral excitations and  $P_s$  transition amplitudes. This procedure is in principle the most exact way to compute  $\Sigma_n^c$ , but gives rise to an algorithm with  $O(N^6)$  complexity.<sup>39,58</sup> However, there is a set of approximate and exact alternatives available to solve Equation (1)<sup>37</sup> that yield the  $O(N^4)$  scaling of the canonical  $G_0W_0$  algorithm.

Leaving the plasmon-pole models<sup>84</sup> aside, there are several full frequency integration techniques available. A popular approach is to compute  $\Sigma_n^c$  on the imaginary axis, where the self-energy integral is smooth and easy to evaluate, and then analytically continue to the real axis. The AC is usually performed by fitting  $\Sigma_n^c(i\omega)$  to a multipole model<sup>68</sup> or by interpolation using a Padé approximant.<sup>41,70</sup> The AC methods produce accurate results for valence states,<sup>41</sup> but fail for core levels, due to the complicated pole structure of the self-energy matrix elements in the deep core region.<sup>22</sup> The CD technique is another full frequency approach, which is suitable for core states and which is described in detail in Section 2.3.

## 2.2 Resolution of the identity

The computation of the self-energy matrix elements  $\Sigma_n^c$  requires the quadrature of the electron repulsion integrals (ERIs) that occur in Equation (5). In this work, these operations are accelerated using the resolution of the identity approximation with the Coulomb metric<sup>60,85</sup> (RI-V). The molecular orbitals (MOs) are expanded in localized atom-centered orbitals  $\{\varphi_\mu\}$ :

$$\Psi_n(\mathbf{r}_i) = \sum_\mu C_{\mu n} \varphi_\mu(\mathbf{r}_i) \quad (11)$$

where  $C_{\mu n}$  are the MO coefficients obtained from the proceeding KS-DFT calculation. In RI we represent the products of MOs in terms of an auxiliary basis set  $\{\phi_P\}$ :

$$\Psi_n(\mathbf{r}_i) \Psi_m(\mathbf{r}_i) = \sum_P A_P^{nm} \phi_P(\mathbf{r}_i) \quad (12)$$

The ERIs can then be expressed as:

$$\begin{aligned} (nm|kl) &= \sum_{PQ} A_P^{nm}(P|Q) A_Q^{kl} \\ (P|Q) &= \int \phi_P(\mathbf{r}_1) v(\mathbf{r}_1, \mathbf{r}_2) \phi_Q(\mathbf{r}_2) d\mathbf{r}_1 d\mathbf{r}_2 \end{aligned} \quad (13)$$

In RI-V, the tensors  $A_P^{nm}$  are obtained by minimizing the  $L_2$  norm of the RI error of the four center integrals.<sup>60,85</sup> We can then present the working equations of RI-V:

$$\begin{aligned} (nm|kl)_{\text{RI-V}} &= \sum_{PQ} (nm|P)(P|Q)^{-1}(Q|kl) \\ &= \sum_R \left\{ \sum_P \sum_{\mu\nu} (\mu\nu|P) C_{\mu n} C_{\nu m} (P|R)^{-\frac{1}{2}} \right. \\ &\quad \times \left. \sum_Q \sum_{\lambda\gamma} (R|Q)^{-\frac{1}{2}} C_{\lambda k} C_{\gamma l} (Q|\lambda\gamma) \right\} \quad (14) \\ &= \sum_R \sum_{\mu\nu} M_R^{\mu\nu} C_{\mu n} C_{\nu m} \times \sum_{\lambda\gamma} M_R^{\lambda\gamma} C_{\lambda k} C_{\gamma l} \\ &= \sum_R O_R^{nm} O_R^{kl} \end{aligned}$$

with the three-center quantities

$$M_P^{\mu\nu} = \sum_R (\mu\nu|R)(R|P)^{-1/2} \quad (15)$$

and their transformation in the MO basis

$$O_P^{nm} = \sum_{\mu\nu} M_P^{\mu\nu} C_{\mu n} C_{\nu m} \quad (16)$$

where the Greek letter indexes  $\mu, \nu, \lambda, \gamma$  refer to the atom-centered orbitals of the primary basis. The effective scaling of the RI-V approximation is  $O(N^3)$ . The memory requirements and prefactor of the algorithm also get dramatically

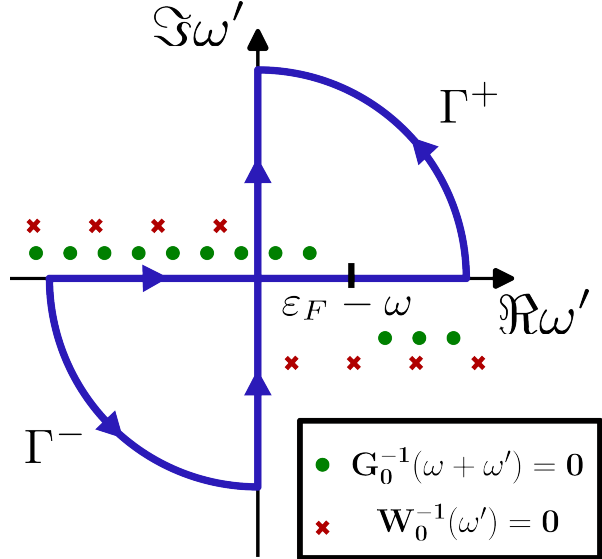


**Figure 1:** Integration path employed for the complex quadrature of the self-energy matrix elements  $\Sigma_n(\omega)$  in the CD method. By design, only some of the poles of  $G_0(\omega + \omega')$  (green dots) lay inside the bounded region, and none of the  $W_0(\omega')$  poles (red crosses).

reduced,<sup>60</sup> as one only needs to compute three and two center integrals, and only the  $O_R^{nm}$  tensors are stored.

## 2.3 Contour deformation technique

The CD technique<sup>22,86,87</sup> has been successfully applied to both valence and core electrons. To name but a few recent applications, consult Refs. 22,48,54,71,88,89. Moreover, we showed for deep core states that the CD self-energies exactly match the fully analytic results from Equation (10).<sup>22</sup> A full derivation of the CD approach in combination with RI-V has been given in our previous work.<sup>22</sup> We summarize in the following the basic idea and the final expressions.

The central idea of the method is to compute the self-energy on the real frequency axis using an integration contour that minimizes the amount of residues inside the bounded area. In particular, all poles of  $W$  lay outside of it and only some poles of  $G$  enter the first or third quadrants. The chosen contour is represented in Figure 1. An application of Cauchy's residue theorem and Jordan's lemma for the  $\Gamma^+$  and  $\Gamma^-$  arcs readily gives:

$$\Sigma^c(\mathbf{r}_1, \mathbf{r}_2, \omega) = -I^c(\mathbf{r}_1, \mathbf{r}_2, \omega) + R^c(\mathbf{r}_1, \mathbf{r}_2, \omega) \quad (17)$$

with the definitions:

$$I^c = -\frac{1}{2\pi} \int_{-\infty}^{+\infty} d\omega' G_0(\mathbf{r}_1, \mathbf{r}_2, \omega + i\omega') W_0^c(\mathbf{r}_1, \mathbf{r}_2, i\omega') \quad (18)$$

$$R^c = - \sum_j^{\text{occ}} \Psi_j(\mathbf{r}_1) \Psi_j^*(\mathbf{r}_2) W_0^c(\mathbf{r}_1, \mathbf{r}_2, \epsilon_j - \omega + i\eta) \theta(\epsilon_j - \omega) \\ + \sum_a^{\text{virt}} \Psi_a(\mathbf{r}_1) \Psi_a^*(\mathbf{r}_2) W_0^c(\mathbf{r}_1, \mathbf{r}_2, \epsilon_a - \omega - i\eta) \theta(\omega - \epsilon_a) \quad (19)$$

Using the RI-V approximation, we can compute the corresponding matrix elements  $I_n^c$  and  $R_n^c$  as follows:

$$I_n^c(\omega) = \frac{1}{2\pi} \sum_m \int \frac{W_{nm}^c(i\omega') d\omega'}{\omega + i\omega' - \epsilon_m - i\eta \operatorname{sgn}(\epsilon_F - \epsilon_m)} \quad (20)$$

$$R_n^c(\omega) = \sum_m f_m W_{nm}^c(|\epsilon_m - \omega| + i\eta) \quad (21)$$

where the factors  $f_m$  are defined in terms of Heaviside step functions:

$$f_m = -\theta(\epsilon_F - \epsilon_m) \theta(\epsilon_m - \omega) + \theta(\epsilon_m - \epsilon_F) \theta(\omega - \epsilon_m) \quad (22)$$

and the matrix elements  $W_{nm}^c$  are computed for an arbitrary complex argument  $\omega$  as:

$$W_{nm}^c(\omega) = \sum_{PQ} O_P^{nm} \Lambda_{PQ}(\omega) O_Q^{mn} \quad (23)$$

with

$$\Lambda = [\mathbf{I} - \Pi(\omega)]^{-1} - \mathbf{I} \quad (24)$$

In Equation (24), we have introduced the polarizability matrices:

$$\Pi_{PQ}(\omega) = \sum_{ia} O_P^{ia} \left[ \frac{1}{\omega - (\epsilon_a - \epsilon_i) + i\eta} + \frac{1}{-\omega - (\epsilon_a - \epsilon_i) + i\eta} \right] O_Q^{ia} \quad (25)$$

Finally, the self-energy matrix elements needed to compute the QP energies in Equation (8) are:

$$\Sigma_n(\omega) = \Sigma_n^x + R_n^c(\omega) - I_n^c(\omega) \quad (26)$$

Compared to the AC of the self-energy, the complexity of the CD algorithm is the same with a bit larger prefactor, whereas for core states the scaling with respect to system size increases by an order of magnitude. The culprit is the residue term  $R_n$ , which becomes the computational bottleneck in core-level calculations, see Section 5.5 for a detailed time complexity analysis.

## 2.4 CD-WAC: Analytic continuation of $\mathbf{W}$

AC techniques are ubiquitous in  $GW$ , but only for the treatment of the self-energy matrix elements. However, they can be used for any meromorphic function, such as the screened Coulomb interaction matrices. Motivated by previous works from Friedrich<sup>77</sup> and Duchemin *et al.*,<sup>49</sup> the idea of the CD-WAC method is to perform an AC of the  $W_{nm}^c(|\epsilon_m - \omega| + i\eta)$

matrices in the  $R_n^c$  term in Equation (21). The strategy for performing the AC of  $W$  is in principle equivalent to that of the self-energy. We compute  $W_{nm}^c$  for a set of imaginary or complex reference frequency points and continue to the real axis.

$W_{nm}^c$  is a quantity that has singularities, i.e. poles at certain frequencies. We use here Padé approximants<sup>90</sup> to derive analytic multipole models for  $W_{nm}^c$ . Padé approximants of order  $M$  are rational functions of the form:

$$T^M(z) = \frac{A_0 + A_1 z + \cdots + A_p z + \cdots + A_{\frac{M-1}{2}} z^{\frac{M-1}{2}}}{1 + B_1 z + \cdots + B_p z + \cdots + B_{\frac{M}{2}} z^{\frac{M}{2}}} \quad (27)$$

where  $A_p$  and  $B_p$  denote complex coefficients. Equation (27) can be represented as a continued fraction,<sup>91</sup> i.e., an expression of the form  $a_1 + 1/(a_2 + 1/(a_3 + 1/(a_p + \cdots)))$  for some other complex coefficients  $a_p$ . Using the form of a continued fraction offers computational advantages, as it enables the use of recurrence formulas in place of explicit polynomial fitting.<sup>92</sup> Moreover, recurrence formulas are favorable as their computation can be carried out efficiently using dynamic programming techniques, such as memoization.

We employ a variant of Thiele's reciprocal differences' algorithm<sup>93</sup> for the interpolation using the continued fraction. The approximant  $T_{nm}^M(z)$  of order  $M$  is defined as:

$$W_{nm}^c(z) \approx T_{nm}^M(z) = \frac{a_1}{1 + \frac{a_2(z^2 - \tilde{z}_1^2)}{1 + \frac{a_3(z^2 - \tilde{z}_{p-1}^2)}{1 + \frac{a_p(z^2 - \tilde{z}_p^2)g_{p+1}(z)}{1 + \frac{\ddots}{\ddots 1 + a_M(z^2 - \tilde{z}_{M-1}^2)}}}}} \quad (28)$$

where  $z$  is a complex argument,  $a_p$  are complex coefficients which need to be determined, and  $\{\tilde{z}_p\}$  is a set of (possibly complex) frequencies for which we compute the reference  $W_{nm}^c$  matrix elements. For the sake of completeness, the equivalence between Equations (27) and (28) is described in detail in Section 2 of the Supporting Information (SI).

For a given set of  $M$  reference frequencies, the following equalities hold:

$$T_{nm}^M(\omega_i) = W_{nm}^c(\omega_i) \quad i = 1, \dots, M \quad (29)$$

The coefficients  $a_i$  can be efficiently computed by recursion,<sup>91</sup> as follows:

$$a_i = g_i(\omega_i) \quad i = 1, \dots, M \quad (30)$$

where the functions  $g_p(z)$  are given by:

$$g_p(\omega_i) = \begin{cases} W_{nm}^c(\omega_i) & p = 1 \\ \frac{g_{p-1}(\omega_{p-1}) - g_{p-1}(\omega_i)}{(\omega_i^2 - \omega_{p-1}^2)g_{p-1}(\omega_i)} & p > 1 \end{cases} \quad (31)$$

and the index  $p$  runs in the range  $1, \dots, M$ .

The argument  $z$  is squared in order to enforce the parity of the screened Coulomb interaction,<sup>49</sup> which is an even function of the frequency  $W(\omega) = W(-\omega)$ . Squaring the argument disrupts the appropriate asymptotic behavior of the approximant, which should converge to zero for extremely large frequencies (see Equations (23) to (25)). Indeed, in the limit of infinite frequency argument, the fraction  $T_{nm}^M(z)$  will only tend to zero for even  $M$ , and will yield a finite non-zero constant for odd  $M$ . However, we compute QP energies for real-world systems with finite core-level binding energies of several hundred or several thousand electronvolts. In practice, we observe that interpolations derived from specific regions of the complex plane yield highly precise results. Further details can be found in the discussion in Section 5.2.

### 3 Implementation details

#### 3.1 Basis sets

The treatment of deep core level requires the usage of basis sets that are able to represent the rapid oscillations occurring within the wave function near the atomic nuclei. For this reason, the CD-WAC method has been implemented in the FHI-aims all-electron software package,<sup>94,95</sup> building on our previous CD implementation.<sup>22</sup> In FHI-aims, the MOs are represented as linear combinations of numerical atom-centered orbitals (NAOs), which are of the general form:<sup>94</sup>

$$\varphi_{i[lm]}(\mathbf{r}) = \frac{u_i(r)}{r} Y_{lm}(\Omega) \quad (32)$$

where  $u_i$  is a radial function, and  $Y_{lm}(\Omega)$  represents the real ( $m \geq 0$ ) and imaginary ( $m < 0$ ) parts of complex spherical harmonics.<sup>96</sup> We remark here that Gaussian type orbitals (GTOs) or Slater type orbitals (STOs) can be also used in FHI-aims, and as can be inferred from Equation (32), they can be considered a special case of the NAOs.

#### 3.2 Padé approximant construction

While the interpolation algorithm used to compute the Padé approximant of  $W$ , as outlined in Equations (28)-(31), is computationally efficient, it is susceptible to numerical instability.<sup>97</sup> The numerical errors in the QP energies are found to be 100 meV larger on average for core levels than for valence states. This is due to two key reasons: i) the complex pole

```

j = maxloc(Wnmc)
z1 = ωj
a1 = g1(z1) = Wnmc(ωj)
for i ← 2 to M do
| j = mink ∈ Nrem |Tnmi(ωk | z1, ..., zi-1, a1, ..., ai-1) - Wnmc(ωk)|
| zi = ωj
| ai = gi(zi)
end

```

**Figure 2:** Greedy implementation of the Thiele's reciprocal differences' algorithm. The intrinsic procedure `maxloc` returns the index of the maximum of the input array. Arguments appearing after the pipe symbol (|) are constant parameters in the function call. See the main text for a discussion of the algorithm steps.

structure necessitates the use of more interpolation points, and ii) the larger reference frequencies associated with core levels, which are squared in the computation of the  $g_p(\omega_i)$  matrices, may introduce potential precision loss in the calculation.

The numerical instabilities can be mitigated by modifying the sequence in which the reference points are incorporated into the interpolation, as indicated in prior work.<sup>98,99</sup> Utilizing this approach, we have successfully stabilized the calculation of the Padé approximant and implemented the method using the greedy algorithm depicted in Figure 2.

Greedy algorithms make the locally optimal choice at each step, and this becomes apparent in our procedure: giving a number of reference frequencies  $M$ , the convergents  $T_{nm}^i$  are constructed by selecting in each iteration the next reference frequency point  $z_i$  from the set of  $N_{\text{rem}}$  remaining points not already included in the convergent  $T_{nm}^{i-1}$ . The heuristic criterion that we employed is to select always the  $\omega_k$  that minimizes the  $L_1$  error between the current convergent and the reference matrix value  $W_{nm}^c(\omega_k)$ . In the first iteration step, we always chose the maximum value of  $W_{nm}^c$  as it accounted for better results in the interpolations. We find that our algorithm improves the quality of the QP energies by two orders of magnitude with respect to the standard Thiele's reciprocal differences approach. The results can be further improved by using multiple precision arithmetic, but this implies the use of external libraries that might add technical overhead to the development process, and it is technically more involved than our simpler approach.

#### 3.3 Choice of reference point

CD-WAC requires a set of reference frequencies  $\mathcal{F}_{\text{wac}}$  and the corresponding reference matrix elements  $W_{nm}^c$ . We have established a heuristic procedure to select  $\mathcal{F}_{\text{wac}}$ , which is displayed in Figure 3. First, due to the parity of the screened Coulomb interaction function, we only consider points on the first quadrant of the complex plane. Depending on the

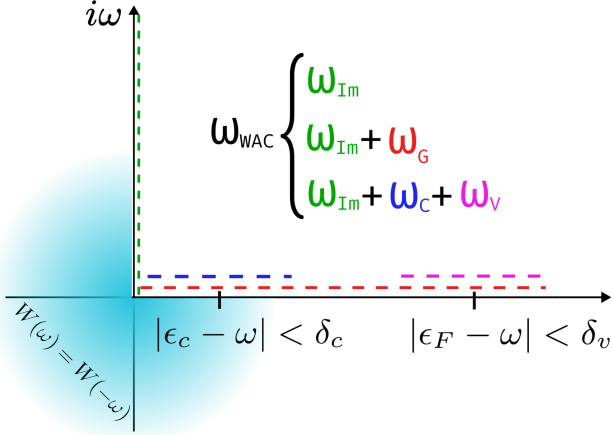


**Figure 3:** Selection of the reference frequency points for the CD-WAC algorithm. The real axis spans the residues  $|\epsilon_m - \omega|$ , and the imaginary axis encompasses the grid used for the numeric integration in  $I_n^c(\omega)$ . The  $\delta_c$  and  $\delta_v$  parameters control the radii of neighborhoods centered at a typical core level residue  $|\epsilon_c - \omega|$  and at  $|\epsilon_F - \omega|$  respectively.

electronic level studied and the target accuracy, three different regions can be used:

- **Valence states:** we reuse the matrix elements  $W_{nm}(i\omega)$  needed for the numerical integration in the  $I_n^c$  term in Equation (26). These are already computed using the set of imaginary frequencies  $\mathcal{F}_{\text{Im}} = \{\omega_{\text{Im}}\}$ . We do not add any extra points.  $\mathcal{F}_{\text{wac}} = \mathcal{F}_{\text{Im}}$
- **Core states, generic settings:** we add to the set of frequencies  $\mathcal{F}_{\text{Im}}$  additional complex points infinitesimally closed to the real axis  $\mathcal{F}_{\text{real}} = \{\omega_G\}$ , using a grid that spans all the possible residues values up to the Fermi level. The complex part of the additional frequencies is chosen to be a small constant (approx  $10^{-3}$  a.u.), which does not affect the results as long as it is small enough.  $\mathcal{F}_{\text{wac}} = \mathcal{F}_{\text{Im}} \cup \mathcal{F}_{\text{real}}$
- **Core states, refined settings:** we add to the set of frequencies  $\mathcal{F}_{\text{Im}}$  additional complex points infinitesimally closed to the real axis spanning two different regions  $\mathcal{F}_{\text{real}} = \{\omega_C\} \cup \{\omega_V\}$ . The first region is a neighborhood centered on a typical core-level residue  $|\epsilon_c - \omega|$ . The second one is a neighborhood centered on  $|\epsilon_F - \omega|$ , representative for a valence-level residue. The radii of the neighborhoods ( $\delta_c, \delta_v$  respectively) are parameters that can be tuned for improving the interpolation results.

The purpose of introducing next to generic the refined settings is to minimize the prefactor of the CD-WAC approach and also to increase accuracy by selecting the most relevant

reference points, see Section 5.1 for comprehensive convergence tests. In what follows, we denote the amount of points in the sets  $\{\omega_C\}$ ,  $\{\omega_V\}$ , and  $\{\omega_{\text{Im}}\}$  as  $N_{\text{core}}$ ,  $N_{\text{valence}}$ , and  $N_{\text{Im}}$  respectively. We also introduce the notation CD-WAC( $N_{\text{core}}$ ,  $N_{\text{valence}}$ ,  $N_{\text{Im}}$ ) to denote a CD-WAC calculation carried out with the specified amount of reference frequencies in the corresponding regions.

### 3.4 CD-WAC procedure

Figure 4 shows both the CD and CD-WAC algorithm for a  $G_0W_0$  calculation. The differences between the two approaches are highlighted in cyan. We start by defining the `wmatrix` procedure which takes a set  $\mathcal{F}$  of frequency points as input and computes the corresponding  $W_{nm}^c$  matrix elements. Both methods start then with the computation of  $W_{nm}^c(i\omega)$ , using a set of imaginary frequencies  $\mathcal{F}_{\text{Im}}$ . The next step is exclusive to CD-WAC: the additional real frequency points are selected, followed by the computation of  $W_{nm}^c(\mathcal{F}_{\text{real}})$ . The AC is performed by the AC procedure, which implements the greedy algorithm in Figure 2. We use in this procedure the  $M$  frequencies contained in the set  $\mathcal{F}_{\text{wac}}$  and the corresponding matrices  $W_{nm}^c(\mathcal{F}_{\text{wac}})$ . Next, given a number of states  $N_{\text{states}}^{\text{CD}}$  to be treated with CD, the QP equation is solved for each one of them as a fixed point iteration with a certain accuracy threshold. The computation of the  $I_n^c(\epsilon'_n)$  term is carried out in the same fashion for both CD and CD-WAC. We perform a numerical integration and sum up over  $m$  up to the full number of states  $N_{\text{states}}^{\text{ALL}}$ .

The second important difference between both approaches arises in the computation of the  $R_n^c(\epsilon'_n)$  term, also highlighted in cyan in the algorithm. For the set  $\mathcal{F}_{\text{res}}$  of residues specified by Equation (22), the CD method computes the matrices  $W_{nm}^c(\omega')$  for the residue  $\omega'$  using the procedure `wmatrix`, whereas CD-WAC employs the already constructed approximant  $T_{nm}^M(\omega')$ . This step of the algorithm is in CD calculations of core excitations the computational bottleneck. With the introduction of CD-WAC, this step is practically free, albeit at the cost of increasing the prefactor of the procedure before the start of the QP iteration (first cyan box). As a final step, the self-energy matrix elements  $\Sigma_n(\epsilon'_n)$  are computed using  $R_n^c(\epsilon'_n)$  and  $I_n^c(\epsilon'_n)$ . Subsequently, they are employed in the update of the QP energies.

Our implementation is designed to be high-performance and capable of handling massive parallelism, making it suited for large scale computations. We leverage distributed parallelism as our primary programming model, maximizing efficiency and scalability. This is achieved by incorporating both established libraries such as ScLAPACK<sup>100</sup> and our own implementation of block cyclic distributions. The latter employs Message Passing Interface<sup>101</sup> (MPI) for performing matrix multiplication.

## 4 Computational details

All  $GW$  and underlying DFT calculations are carried out with the FHI-aims program package.<sup>94</sup> For the frequency integration of the  $GW$  self-energy, we use the CD and CD-WAC techniques. In both cases, the imaginary axis integral (Equation (20)) is solved by quadrature using a modified Gauss-Legendre grid<sup>60</sup> of 200 points.

Two benchmark sets are employed to verify the accuracy of CD-WAC with respect to CD, namely CORE65<sup>47</sup> and GW100.<sup>41</sup> The former includes 65 1s core level excitation energies of 32 organic molecules containing the H, C, N, O, and F atoms. The latter reports HOMO and LUMO QP energies from 100 closed-shell molecules covering a wide range of ionization potentials. The performance of the new implementation was studied using small-medium size organic molecules, in particular we used acene chains<sup>22</sup> of the type  $(C_{4n+2}H_{2n+4})_{n=1,\dots,15}$ , and a hydrogenated amorphous carbon material<sup>24</sup> with the elemental composition a-C<sub>46</sub>H<sub>70</sub>.

The CORE65 benchmark calculations are performed with different  $GW$  flavors. These are i) single-shot  $G_0W_0$  using an optimized starting point, ii) partial and iii) full eigenvalue-self-consistent schemes and iv) a Hedin-shift in the Green's function. We denote the partial eigenvalue-self-consistent scheme as  $evGW_0$  and the full eigenvalue-self-consistent as  $evGW$ . In  $evGW_0$ , the eigenvalues are only updated in  $G$ , while in  $evGW$  the eigenvalues are updated in  $G$  and  $W$ . The Hedin shift approximates the  $evGW_0$  scheme by introducing a shift  $\Delta H_n$  in the denominator of  $G$ . The shift  $\Delta H_n$  is separately determined for each core-level  $n$  before starting the iteration of the QP equation (Equation (8)). This approach was comprehensively described in Ref. 54 and we refer to it as  $G_{\Delta H}W_0$  in the following.

We use the Perdew-Burke-Ernzerhof (PBE) functional<sup>102</sup> as DFT starting point for the core-level calculations with  $evGW_0$ ,  $evGW$  and  $G_{\Delta H}W_0$ . The core-level  $G_0W_0$  calculations are performed on-top of the PBEh( $\alpha$ ) hybrid functional<sup>103</sup> with 45% of exact exchange ( $\alpha = 0.45$ ), which was previously optimized to match the  $evGW_0$ @PBE reference and experimental XPS data.<sup>47</sup> For the valence-level excitations, we use  $G_0W_0$ @PBE as in the original GW100 benchmark paper.<sup>41</sup>

Relativistic effects were included for all core-level calculations by adding a corrective term derived in Ref. 48 to the non-relativistic  $GW$  QP energies. The CORE65 and amorphous carbon calculations use the Dunning basis sets family<sup>104,105</sup> cc-pVnZ with  $n \in [T, Q]$ . In the case of GW100 and the acene chains, we employ the def2-QZVP basis set.<sup>106</sup> The cc-pVnZ and def2-QZVP are contracted Gaussian basis sets, which can be considered as a special case of an NAO and which are then treated numerically in FHI-aims. The self-energy and screened Coulomb interaction calculations for the H<sub>2</sub>O molecule were carried out using both the

```

Procedure wmatrix( $\mathcal{F}$ ):
  | foreach  $\omega \in \mathcal{F}$  do
  |   |  $\Lambda(\omega) = [\mathbf{I} - \Pi(\omega)]^{-1} - \mathbf{I}$ 
  |   |  $W_{nm}^c(\omega) = \sum_{PQ} O_P^{nm} \Lambda_{PQ}(\omega) O_Q^{mn}$ 
  |   | end
  | end
  |  $W_{nm}^c(\mathcal{F}_{\text{im}}) = \text{wmatrix}(\mathcal{F}_{\text{im}})$ 
  | if cdwac then
  |   | if real_frequencies then
  |   |   |  $W_{nm}^c(\mathcal{F}_{\text{real}}) = \text{wmatrix}(\mathcal{F}_{\text{real}})$ 
  |   | end if
  |   |  $\mathcal{F}_{\text{wac}} = \mathcal{F}_{\text{im}} \cup \mathcal{F}_{\text{real}}$ 
  |   |  $T_{nm}^M(\omega) = \text{AC}[\omega | \mathcal{F}_{\text{wac}}, W_{nm}^c(\mathcal{F}_{\text{wac}})]$ 
  | end if
  | for  $n \leftarrow 1$  to  $N_{\text{states}}^{\text{CD}}$  do
  |   |  $\epsilon'_n = \epsilon_n$ 
  |   | while  $|\epsilon'_n - \epsilon_n^{G_0W_0}| < \text{threshold}$  do
  |   |   | for  $m \leftarrow 1$  to  $N_{\text{states}}^{\text{ALL}}$  do
  |   |   |   | foreach  $i\omega \in \mathcal{F}_{\text{im}}$  do
  |   |   |   |   |  $k_{nm} = [\epsilon'_n + i\omega - \epsilon_m \pm i\eta]^{-1}$ 
  |   |   |   |   |  $I_n^c(\epsilon'_n) \leftarrow I_n^c(\epsilon'_n) + \int d\omega \frac{k_{nm} W_{nm}^c(i\omega)}{2\pi}$ 
  |   |   |   | end
  |   |   | end
  |   |   | foreach  $\{\epsilon_m - \epsilon'_n\} \in \mathcal{F}_{\text{res}}$  do
  |   |   |   |  $\omega' = |\epsilon_m - \epsilon'_n| + i\eta$ 
  |   |   |   | if cdwac then
  |   |   |   |   |  $W_{nm}^c(\omega') = T_{nm}^M(\omega')$ 
  |   |   |   | else
  |   |   |   |   |  $W_{nm}^c(\omega') = \text{wmatrix}(\omega')$ 
  |   |   |   | end if
  |   |   |   |  $R_n^c(\epsilon'_n) \leftarrow R_n^c(\epsilon'_n) + f_m W_{nm}^c(\omega')$ 
  |   |   | end
  |   |   |  $\Sigma_n(\epsilon'_n) = \Sigma_n^x + R_n^c(\epsilon'_n) - I_n^c(\epsilon'_n)$ 
  |   |   |  $\epsilon_n^{G_0W_0} = \epsilon_n + \Re \Sigma_n(\epsilon'_n) - v_n^{xc}$ 
  |   | end
  |   |  $\epsilon'_n = \epsilon_n^{G_0W_0}$ 
  | end

```

**Figure 4:** The  $G_0W_0$  algorithm using CD and CD-WAC. The cyan regions highlight the differences between both approaches. A detailed description of the quantities computed in each step can be found in the main text.

cc-pVQZ and NAOs of the Tier 1 of quality<sup>94</sup> basis sets. In all cases, RI-V<sup>85</sup> was used. In FHI-aims, the auxiliary basis sets for RI-V are constructed on-the-fly by generating on-site products of primary basis functions, which are then orthonormalized for each atom with a Gram-Schmidt procedure.<sup>60</sup> The input and output files of all the FHI-aims calculations are available in the NOMAD database.<sup>107</sup>

## 5 Results

In the following section, we will analyze our implementation of the CD-WAC method. We will benchmark its accuracy compare to the parent method (CD), and demonstrate that the theoretical speedup is achieved in practice.

### 5.1 CD-WAC sensible defaults

The first step in our CD-WAC study is the selection of the sensible defaults of the method. That is, the settings that should provide accurate results up to a given threshold and that minimize the number of reference matrix elements  $W_{nm}^c$  that must be computed. As decision criterion, we compare the QP energies obtained with CD-WAC to the CD reference.

We start with the defaults for the valence states by assessing the GW100 benchmark set using only the imaginary frequency grid  $\mathcal{F}_{\text{im}}$ . We find that the mean absolute errors (MAE) for both the HOMO and LUMO states with respect to CD are in the range of  $\sim 10^{-4}$  eV, which is further analyzed in Section 5.3. Including only  $\mathcal{F}_{\text{im}}$  in the AC of  $W$  seems to be sufficient for frontier orbitals, which is in agreement with the results of Duchemin and Blase.<sup>49</sup>

For deep core level states, we found that the CD-WAC calculations are more complicated than for valence states, which is also in agreement with the preliminary studies by Duchemin and Blase.<sup>49</sup> They studied the 1s core state of a single H<sub>2</sub>O molecule and proposed to complete the imaginary frequency grid  $\mathcal{F}_{\text{im}}$  with additional complex frequencies very close to the real axis. We employ a similar, but more refined strategy by using the heuristic procedure described in Section 2.4.

We distinguish between generic and refined settings. In the generic brute force approach, the points  $\mathcal{F}_{\text{real}}$  are equidistantly spread, yielding the grid  $\omega_G$ . Using a grid size of 100 points for  $\omega_G$ , we obtain an MAE of 5 meV with respect to CD for the CORE65 benchmarks set. The MAE can be systematically decreased by increasing the size of  $\omega_G$ , see Figure S1. While the generic settings yield accurate results, we aim to reduce the total number of points  $\mathcal{F}_{\text{real}}$  and the number of outliers by using the refined setting with the two different grids  $\{\omega_C\}$  and  $\{\omega_V\}$ .

The optimal amount of points  $N_{\text{core}}$  and  $N_{\text{valence}}$  in the sets  $\{\omega_C\}$  and  $\{\omega_V\}$ , respectively, is determined by computing the MAE with respect to CD for the CORE65 benchmark set at

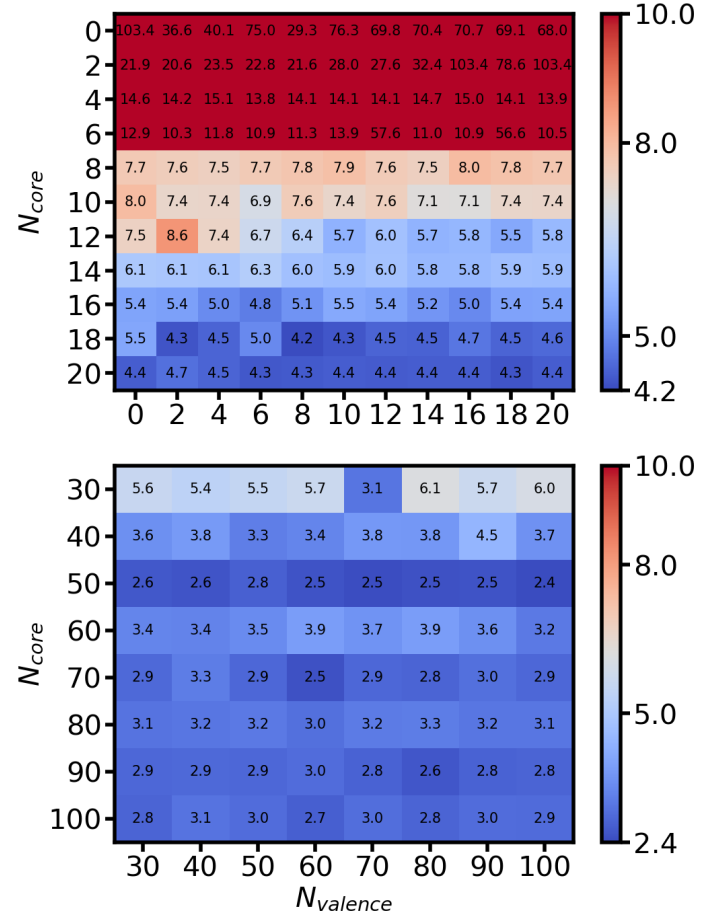


**Figure 5:** MAEs in meV of CD-WAC with respect to CD for the CORE65 benchmark set as a function of the number of additional frequencies  $\mathcal{F}_{\text{real}}$ .  $N_{\text{core}}$  and  $N_{\text{valence}}$  are the number of points in  $\{\omega_C\}$  and  $\{\omega_V\}$ , respectively. The 1s QP energies are computed at the  $G_0 W_0 @ \text{PBEh}(\alpha = 0.45)$  level using the cc-pVTZ basis set.

the  $G_0 W_0 @ \text{PBEh}(\alpha = 0.45)$  level using the cc-pVTZ basis set. Keeping a constant size of the imaginary frequency grid  $N_{\text{Im}} = 200$ , we explored numerous combinations of points from both regions. The corresponding MAEs are included in the heat maps in Figure 5. We studied the progressive increase of  $N_{\text{core}}$  and  $N_{\text{valence}}$  using fine grids up to 20 points (upper heat map in Figure 5), and using coarse grids from 20 to 100 points (lower heat map in Figure 5).

We can see that the MAEs in the coarse grid heat map are quite stable, with no major improvement being observed when going beyond 30 points for any of the two regions. Larger changes are observed for less than 20 points in both  $\{\omega_C\}$  and  $\{\omega_V\}$ . The heat map with the fine grid displays a decrease of the MAE from 0.103 eV to 0.004 eV with increasing grid size. For most systems, using  $N_{\text{core}} \sim 20$  offers the best results. The dependency on  $N_{\text{valence}}$  seems to be weaker, although non negligible, as it systematically improves the results on the fourth decimal. Using the notation CD-WAC( $N_{\text{core}}, N_{\text{valence}}, 200$ ), we recommend CD-WAC(20,

20, 200) as the default settings of the method. The validity of this choice will be reinforced in the next section, when discussing the screened Coulomb interaction and self-energy matrix elements.

## 5.2 Screened Coulomb and self-energy structures

An accurate prediction of the QP energies requires that the CD-WAC method correctly reproduces the matrix elements of the screened Coulomb and ultimately the self-energy. We focus on deep core level matrix elements because i)  $\Sigma_n^c(\omega)$  and  $W_{nm}^c(\omega)$  have a less complicated pole structure for valence states<sup>22</sup> and are easier to reproduce than their core-level counterpart, and ii) the target excitations of this work are deep core states. To facilitate comparison with relevant previous works,<sup>22,49</sup> we compute the screened Coulomb matrix and the self-energy for the oxygen 1s core state of the H<sub>2</sub>O molecule. In addition, we also inspect the influence of the basis set on the obtained curves.

Figure 6 represents the real part of the  $\Sigma_n^c(\omega)$  and  $W_{nm}^c(\omega)$  matrices for  $n, m = O1s$ . We compare our default settings CD-WAC(20, 20, 200) and larger grids CD-WAC(50, 100, 200) with the CD results in every case. The  $G_0W_0$  calculations on the left panel were carried out using a Gaussian basis set (cc-pVQZ). In the right panel, we used NAOs of the first tier of quality. The underlying DFT functional is PBE in all cases. PBE is not used as starting point for core-level calculations with  $G_0W_0$  as discussed in Section 1. However, among the different  $GW$  flavors discussed here, the  $G_0W_0$ @PBE self-energies have typically the most complicated structure in the frequency region where the QP solution is expected. That means if we can reproduce the  $G_0W_0$ @PBE self-energy than, e.g., the one from  $G_0W_0$ @PBEh( $\alpha=0.45$ ) is even more likely to be reproduced well.

The first noticeable difference between CD and CD-WAC is the amplitude of the poles, which differs in both  $\Sigma_n^c$  and  $W_n^c$ . However, this difference is only a numerical artifact introduced by the size of the imaginary component in Equation (25). Indeed, for CD calculations we only have the infinitesimal  $i\eta$ , but for CD-WAC we also have the contribution of the imaginary part of the additional reference frequencies.

More important, we can see that CD-WAC provides a highly accurate position of the poles of both  $\Sigma_n^c(\omega)$  and  $W_{nm}^c(\omega)$  with respect to CD, irrespective of the nature of the basis set employed. Some of the smaller poles are not retrieved though, but considering that the QP energies on this example have absolute errors of  $10^{-4}$  eV, we can conclude that either these features are simply not relevant for our target accuracy or a product of numerical noise introduced by the discontinuous virtual-state spectrum of localized basis sets. These numerical effects are likely related to charge neutral

valence excitations to high energy virtual states, leading to a few additional small poles in the core region. This is an artifact of finite basis sets, and the spectrum in the unoccupied states should become continuous in the infinite basis set limit. In a way, CD-WAC acts like a pruning device that eliminates spurious pole features in  $\Sigma_n^c(\omega)$  and  $W_{nm}^c(\omega)$ , while keeping the desired accuracy. We can also observe that there is little difference in the form of the curves obtained with CD-WAC(20, 20, 200) and those of CD-WAC(50, 100, 200), which further validates our sensible defaults selection.

## 5.3 GW100 and CORE65 benchmarks

In the following, we benchmark the accuracy of the CD-WAC method employing the popular GW100<sup>41</sup> set for frontier orbitals and the CORE65<sup>47</sup> set for 1s excitations. In addition to the MAEs already given in Section 5.1, we analyze their dependence on the different basis sets and excitation types and report the spread of errors.

Figure 7 represent the box plots of the absolute errors between CD and CD-WAC for both GW100 and CORE65. For GW100 we use  $G_0W_0$ @PBE and the def2-QZVP basis set, enabling comparison with the reference data established by Setten *et al.*,<sup>41</sup> and CD-WAC(0,0,200) settings. The HOMO and LUMO energies of the GW100 set have MAEs of the order of  $10^{-4}$  eV, and they have a symmetric, narrow distribution. The very small dispersion is confirmed by the median absolute deviation (MADs) of  $10^{-4}$  eV, which coincides with the MAEs. We also note that our CD and CD-WAC GW100 results deviate on average less than 5 meV from the data in the original GW100 paper,<sup>41</sup> i.e., FHI-aims with analytic continuation using 16 Pade parameters and the Turbomole no-RI results.

All the CORE65 calculations were carried out at the  $G_0W_0$ @PBEh ( $\alpha=0.45$ ) level of theory, using our CD-WAC(20,20,200) default settings. We employ the cc-pVTZ and cc-pVQZ basis sets to explore the influence of increasing basis set size on the approximation. CD-WAC yields with an MAE of 4 meV an excellent accuracy, although the error is one order of magnitude higher than in the valence case. However, the MAEs are nicely preserved when increasing the basis set size. Compared to GW100, the distributions are wider and more skewed, particularly for cc-pVQZ. The medians are for both basis sets very close to the first quartile and the minimum. This implies that the absolute errors are below 4 meV for most 1s excitations, which is more than sufficient for the prediction of core-level excitations.

To further study the distribution of the absolute errors in the CORE65 calculations, we have complemented the box plots with the histograms in Figure 8. These plots indeed confirm that most systems have errors below 4 meV. The histograms additionally show the dependence on the core-

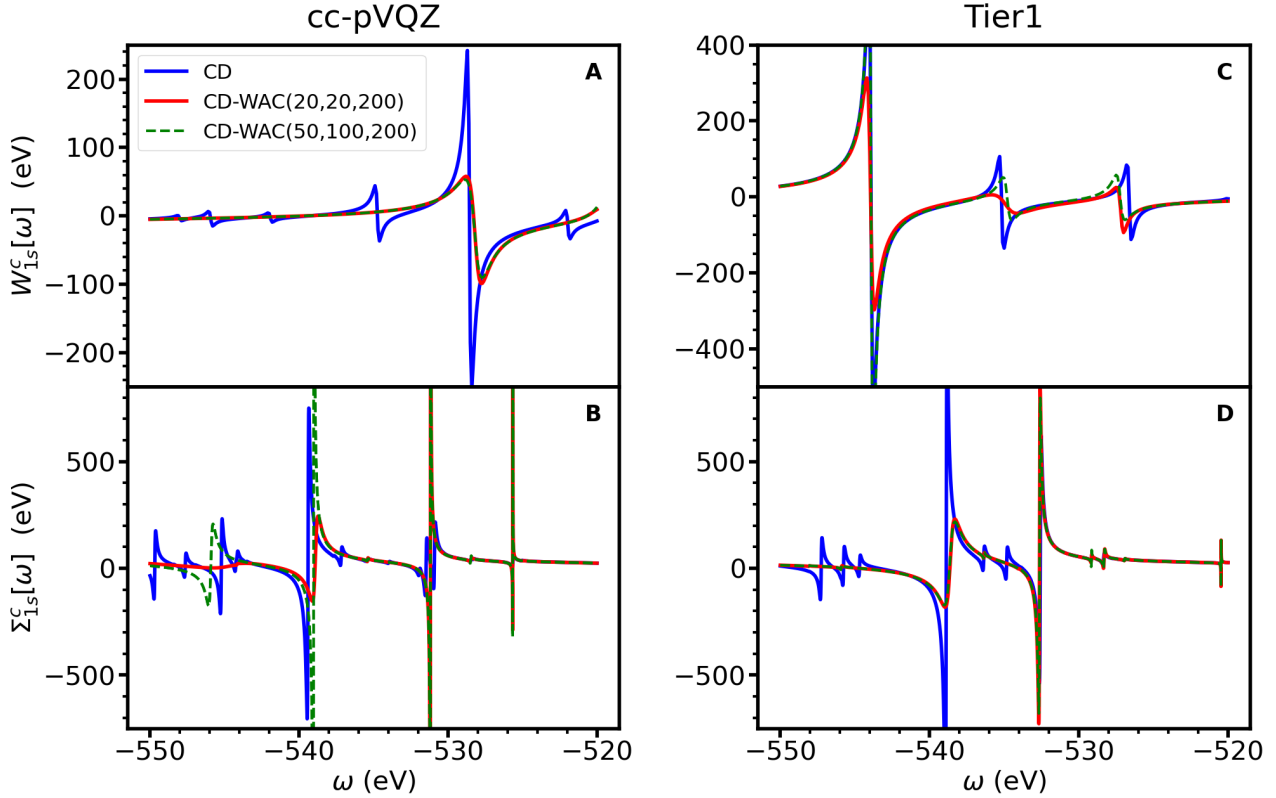


**Figure 6:** Correlation part of the screened Coulomb interaction matrices  $W_{nm}^c(\omega)$  (A, C) and self-energy matrices  $\Sigma_n^c(\omega)$  (B, D) as a function of the frequency for the oxygen 1s core level of the  $\text{H}_2\text{O}$  molecule. The quantities are computed at the  $G_0W_0$ @PBE level using the cc-pVQZ (left panel) and Tier1 basis sets (right panel).

level type. We find that the N1s excitations have more frequently higher errors, while CD-WAC reproduces the O1s states best. This is also supported by Table 1, where the MAEs and MADs are given by excitation type. The subgroup of N1s excitation has for both basis sets MAEs of  $\sim 10$  meV, which is higher than the overall MAE, but still excellent.

Outliers with errors larger 0.017 eV are not displayed in Figure 8. For cc-pVTZ, there are four outliers: three with an error of 0.02 eV and one with 0.07 eV. For cc-pVQZ, we find three outliers with errors between 0.02 eV and 0.06 eV; see SI for details. The smallest chemical shifts for second-row elements, in particular for C1s, are 0.1 eV. We note here that even the largest outliers are below this threshold.

#### 5.4 Beyond $G_0W_0$ calculations

Next, we assess the quality of the CD-WAC approximation for methods beyond  $G_0W_0$ . We performed  $\text{ev}GW_0$ ,  $\text{ev}GW$ , and  $G_{\Delta\text{H}}W_0$  calculations using CD-WAC(20, 20, 200) and compared them with CD. Table 1 contains the MAEs and MADs for each excitation type, as well as the overall values. We remind the reader that the statistics for F1s are rather poor since we have only three of those excitations in the benchmark set, but we included it for the sake of completeness.

Compared to  $G_0W_0$ , the partially self-consistent schemes have larger MAEs. For  $\text{ev}GW$  and  $G_{\Delta\text{H}}W_0$  we observe an increase by an order of magnitude and even two orders of magnitude for  $\text{ev}GW_0$ . A detailed report of the individual core excitations is provided in the Tables S2 and S3 of the Supplementary Information (SI).

Starting the discussion with  $\text{ev}GW$ , we find that the different excitation types have similar MAEs, each  $< 55$  meV. In comparison to  $G_0W_0$ , the MADs are consistently larger by a factor of 10, indicating that also the dispersion of the data increases. The reason for the increase might be attributed to the fact that the PBE self-energies tend to have more features than the ones from a hybrid functional such as PBEh, making it more difficult to reproduce them by CD-WAC.

While the accuracy of CD-WAC is still satisfying for  $\text{ev}GW$ , it is surprisingly large for  $\text{ev}GW_0$ . With an MAE of 0.1 eV, the CD-WAC error touches the experimental resolution of carbon 1s binding energies. The lower errors observed in  $\text{ev}GW$  offer a reason for this impairment. The  $W_{nm}^c$  matrices are recomputed in every iteration of  $\text{ev}GW$  using the perturbed eigenvalues, including the computation of the extra references. This results in a new Thiele interpolant being constructed in each iteration, which compensates for the error introduced in the computation of the updated eigenvalue. However, in  $\text{ev}GW_0$ , only one interpolant is employed for all iterations, leading to an accumulation of error on the

**Table 1:** MAEs and MADs in MeV for CD-WAC with respect to CD using the CORE65 benchmark set and different  $GW$  flavors.

|     | cc-pVTZ                         |                                 | cc-pVQZ                         |                                 | cc-pVTZ |       |       |       |        |         |
|-----|---------------------------------|---------------------------------|---------------------------------|---------------------------------|---------|-------|-------|-------|--------|---------|
|     | $G_0W_0$ @PBEh( $\alpha=0.45$ ) | MAE     | MAD   | MAE   | MAD   | MAE    | MAD     |
| all | 4.408                           | 0.4000                          | 4.315                           | 0.8000                          | 147.7   | 48.92 | 36.81 | 6.450 | 26.25  | 0.4000  |
| C   | 4.700                           | 1.100                           | 3.571                           | 1.400                           | 71.21   | 31.42 | 54.48 | 7.210 | 11.20  | 1.600   |
| N   | 12.41                           | 6.800                           | 14.01                           | 1.150                           | 101.7   | 56.50 | 32.55 | 4.450 | 91.37  | 19.55   |
| O   | 0.4071                          | 0.1500                          | 0.9024                          | 0.3000                          | 257.5   | 57.85 | 17.36 | 5.300 | 17.35  | 0.1000  |
| F   | 0.1417                          | 0.02500                         | 0.06667                         | 0.0000                          | 312.9   | 34.97 | 11.76 | 7.475 | 0.2722 | 0.05000 |

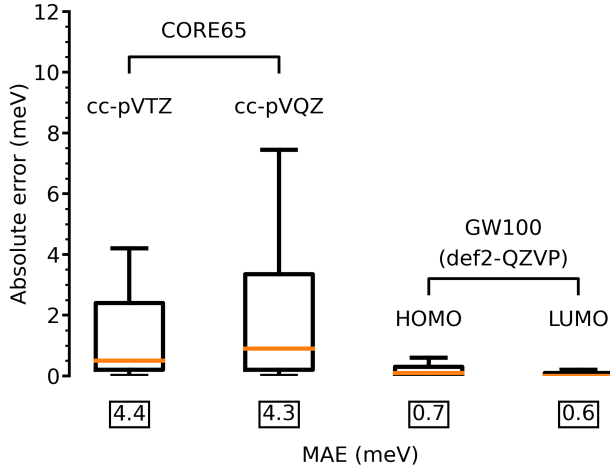


**Figure 7:** Box plots of the absolute errors of the CD-WAC method with respect to CD for the CORE65 and GW100 benchmark sets at the  $G_0W_0$ @PBEh( $\alpha=0.45$ ) and  $G_0W_0$ @PBE level, respectively. The corresponding MAEs and basis sets are also reported. Boxes indicate the "interquartile range" measuring where the bulk of the data are. The median is indicated by an orange line.

perturbed eigenvalue without compensation. Another source of error in  $evGW_0$  is the interpolation vicinity, which for the points in  $\omega_V$  is centered on  $|\varepsilon_F - \varepsilon_m|$ , where  $m$  indexes a core states. However, after some iterations a more adequate center would be  $|\varepsilon_F - \varepsilon_m^{GW}|$  because the difference between KS eigenvalue and QP energy can be easily tens of eV for deep core states.<sup>22</sup> This problem also does not occur in  $evGW$ .

It should be in principle possible to improve the accuracy for  $evGW_0$ . For example, the Pad  approximant could be re-evaluated after some iteration steps with reference points from the  $\omega_V$  region re-centered at  $|\varepsilon_F - \varepsilon_m^{GW}|$ . However, in our recent benchmark study,<sup>54</sup> we proposed the  $G_{\Delta H}W_0$  as an approximation to  $evGW_0$ , which yields the same errors with respect to experiment, but is in terms of computational cost comparable to  $G_0W_0$ . For large systems, we would rather use  $G_{\Delta H}W_0$  or  $G_0W_0$ @PBEh( $\alpha=0.45$ ). For small systems, the CD is computationally affordable, which leaves little incentive to tune the CD-WAC performance for  $evGW_0$ .

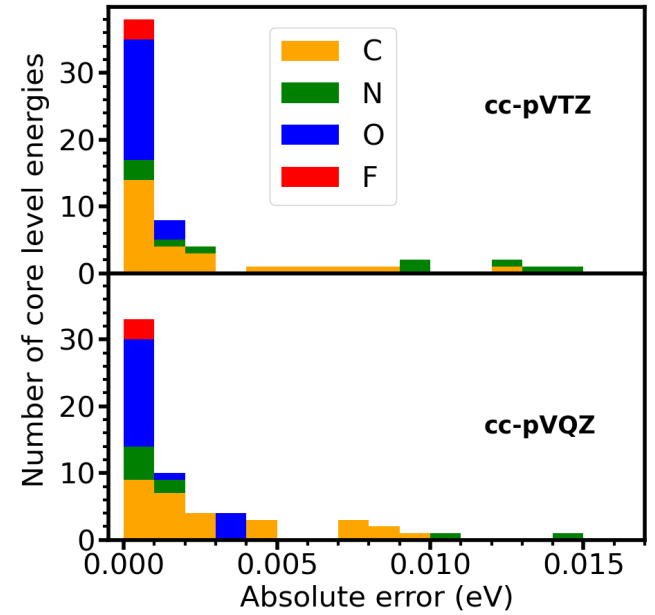


**Figure 8:** Histogram of the absolute errors between CD and CD-WAC per atom type in the CORE65 test set at the  $G_0W_0$ @PBEh( $\alpha=0.45$ ) level using the cc-pVTZ and cc-pVQZ basis sets. Outliers are not included on the plot.

The CD-WAC performance for  $G_{\Delta H}W_0$  is similar to  $evGW$ , yielding MAEs <100 meV. The reason for the decreased accuracy compared to  $G_0W_0$  must be again attributed to the underlying PBE functional, which yields feature-rich self-energy structures. Unlike for  $evGW$ , the MAEs differ between the atom types. In particular, the MAE for the N1s stands out, caused by four outliers with errors between 0.1 – 0.4 eV. Closer inspection of the outliers reveals the CD self-energy has shallow, small poles close to the QP solution, see for example Figure S2.

As already mentioned in Section 5.2, we believe that these poles are artifacts caused by the discontinuous virtual-state spectrum in localized basis functions. They can be associated to charge neutral excitation  $\Omega_s$  from the valence states to the highest virtual states, which occur in the self-energy, see Equation (10). There are several observations that support this interpretation: i)  $\Omega_s$  are close to eigenvalue differ-

ences. For the outliers, the highest virtual states are indeed in the range of the N1s binding energies with cc-pVTZ. This also explains why the other excitation types are not affected. ii) We observe these spurious poles more frequently with an underlying PBE functional than with PBEh.  $\Omega_s$  are underestimated at the PBE, but overestimated at the PBE level, shifting them out of the frequency range of the QP solution. iii) The number of these spurious poles increases with the basis set size because, e.g., the cc-pV5Z and cc-pVQ6Z basis sets span virtual states up to several thousand eV, see also the SI of Ref. 47, where we briefly discussed this issue discussed as cause for the disturbance in the basis set extrapolation. CD-WAC prunes this spurious poles and arguably yields the better result for localized basis functions.

## 5.5 Performance of the implementation

The key feature of the CD-WAC approach is the reduction of the computational requirements of the standard CD approach by finding an analytical model for the residue term  $R_n^c$  (Equation (21)). In the valence case, we showed that it is sufficient to include only the imaginary frequency points for the analytic continuation of  $W$ , which implies re-using the  $W_{mn}(i\omega)$  matrix elements that we compute anyway for the  $I_n^c$  term (Equation (20)). For the HOMO, one typically has to compute one or two residues independent of the system size. Thus, CD-WAC saves the computation of  $W_{mn}$  for two (real) frequency points. This corresponds to a marginal prefactor reduction compared to CD: Assuming we have an imaginary frequency grid of 100 or 200 points and that the system is large enough for the  $W_{mn}$  evaluation to dominate the computational cost, then CD-WAC saves at best 1% of the total computational time.

The situation is completely different for core states, for which the CD-WAC methods reduces the scaling by one order of magnitude from  $O(N^5)$  to  $O(N^4)$ . We demonstrate the latter by conducting  $G_0W_0$ @PBEh( $\alpha=0.45$ ) calculations for a series of acene chains ( $C_{4n+2}H_{2n+4}$ ) $_{n=1,\dots,13,15}$  using CD-WAC(100, 0, 100), i.e., generic settings. Figure 9 displays the execution time for the  $GW$  calculation, excluding the preceding DFT calculation and the cubic scaling computation of the RI integrals (Equation (16)). The complexities of both the CD and CD-WAC calculations precisely agree with the theoretical predictions and match the results of previous studies in the case of CD.<sup>22</sup>

To understand the origin of the scaling laws, we need to consider the  $I_n^c$  and  $R_n^c$  terms independently. In both CD and CD-WAC, the numerical quadrature of the integral  $I_n^c$  is performed by using, e.g., a modified Gauss-Legendre grid with  $N_\omega$  points. The grid size is practically independent of the system size.<sup>60</sup> The scaling of the quadrature will be dominated by the computation of the matrix elements  $\Pi_{PQ}(i\omega)$ . Formally, this requires  $N_\omega N_{\text{occ}} N_{\text{virt}} N_{\text{aux}}^2$  operations, where

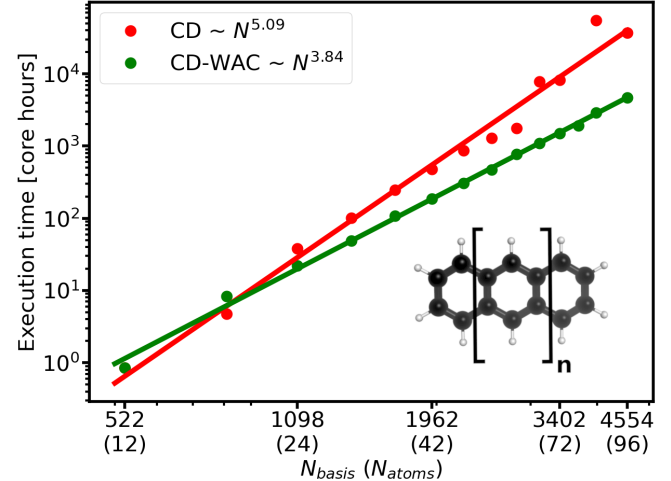


**Figure 9:** Performance of the CD-WAC implementation compared with CD. The plots report the execution time of the  $GW$  part for acene chains from 2-14,15 rings using the def2-QZVP basis set. The solid lines represent the two-parameter least-squares fits of prefactor and exponent. The latter is reported in the legend of the plot. Calculations performed with Intel Xeon Platinum 8168 CPUs at 2.7 GHz.

$N_{\text{occ}}$  and  $N_{\text{virt}}$  are the number of occupied and virtual states, respectively, and  $N_{\text{aux}}$  is the number of auxiliary (RI) basis functions. This leads to a  $O(N^4)$  complexity for the  $I_n^c$  term because  $N_{\text{occ}}$ ,  $N_{\text{virt}}$  and  $N_{\text{aux}}$  increase linearly with system size.

The computation of the  $R_n^c$  term is dominated by  $\Pi_{PQ}(|\epsilon_m - \omega|)$  as previously shown in Ref. 22. In the CD implementation, this requires  $N_{\text{res}} N_{\text{occ}} N_{\text{virt}} N_{\text{aux}}^2$  operations, where  $N_{\text{res}}$  are the number of residues entering the summation in equation (21). For valence states, this number is usually small and independent of the system size, as discussed above, and the overall scaling is  $O(N^4)$ . For deep core states, however, it is of the order  $N_{\text{res}} \sim N_{\text{occ}}$ , which gives rise to the unfavorable scaling of  $O(N^5)$ . This can be understood by inspecting the arguments of  $\Pi_{PQ}$  in  $R_n^c$  and  $I_n^c$  in equations (21) and (20). For  $R_n^c$ , the argument of  $\Pi_{PQ}$  depends on the index  $m$ , which runs over the number of residues, whereas we have a dependency on an imaginary grid of constant size  $N_\omega$  in  $I_n^c$ . When the analytic continuation of  $W$  is carried out for  $R_n^c$ , the computational time for evaluating the latter is negligible during the iteration of the QP equation (8). The computational cost in CD-WAC is hence dominated by the  $I_n^c$  term and the quartic scaling computation of  $W_{mn}^c$  for the additional real frequencies  $\mathcal{F}_{\text{real}}$ . Since the number of extra points is independent on the system size, the total scaling of CD-WAC is consequently  $O(N^4)$ .

The calculation of  $W_{mn}^c$  for the additional real frequencies adds to the prefactor in the CD-WAC algorithm. For small systems, the number of residues (times the number of iteration steps of equation (8)) is smaller than the additional WAC frequencies. In this case, CD is faster than CD-WAC. How-

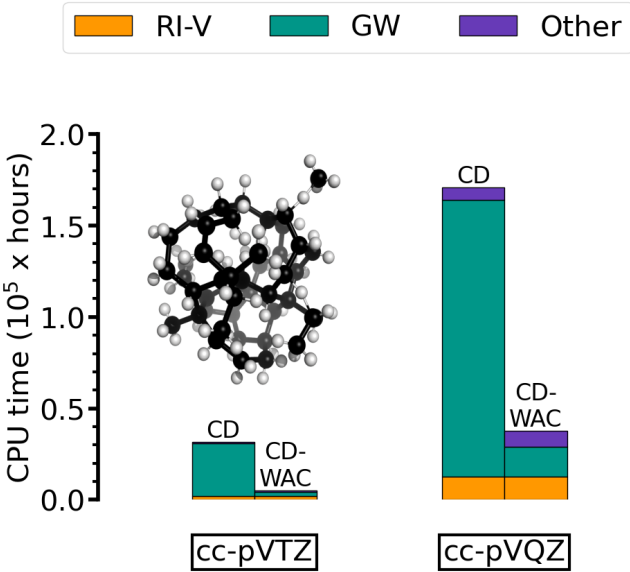


**Figure 10:** Comparison of the total run time (CPU hours) for the computation of the C1s excitation of the central atom in the amorphous carbon cluster  $a\text{-C}_{46}\text{H}_{70}$  using CD and CD-WAC(20, 20, 200). The absolute errors (CD vs. CD-WAC) for the cc-pVTZ and cc-pVQZ are 0.3 meV and 0.4 meV, respectively. Calculations performed with Intel Xeon Platinum 8168 CPUs at 2.7 GHz.

ever, the cross-over between CD and CD-WAC occurs already around 16 atoms as shown in Figure 9, where generic CD-WAC settings with 100 extra points are used. With our optimized settings, only 40 additional points are required, which moves the cross-over point between CD and CD-WAC to even smaller systems.

Next, we investigate the performance improvement for the total run times, including now also the DFT part and the calculation of the 3-center RI quantities  $O_p^{nm}$  (Equation (16)). The 3-center quantities are computed before the SCF cycle starts. They enter the computation of the exchange energy in hybrid DFT and are then also used in the polarizability and *GW* self-energy. As detailed in our previous work,<sup>22</sup> the RI integral evaluation has a cubic time complexity, but it has potentially a large prefactor dependent on the type of basis function treated in our NAO scheme. The 3-center RI integral can significantly contribute to the total time, while the overhead due to other computation steps in the DFT part is marginal. In the following, we discuss therefore only the RI and *GW* self-energy evaluation as relevant contributions.

We investigate the CD-WAC speed-up for the total execution time for a production-run system, namely an amorphous carbon cluster of 116 atoms ( $a\text{-C}_{46}\text{H}_{70}$ ). The  $a\text{-C}_{46}\text{H}_{70}$  cluster is part of the *GW* training data, which we used to develop a machine-learning model for XPS predictions of disordered carbon materials.<sup>24</sup> Figure 10 shows the total execution time for the spin-polarized calculation of the C1s excitation of the central carbon atom in the cluster. We compare

CD and CD-WAC(20, 20, 200) and indicate with different colors the RI and *GW* contributions to the run time. The settings are the same as in our previous work,<sup>24</sup> i.e. Dunning basis sets and  $G_0W_0$ @PBEh( $\alpha = 0.45$ ). CD-WAC speeds-up the *GW* self-energy evaluation by a factor of 12.6 and 9.2 for cc-pVTZ and cc-pVQZ, respectively. The RI part, which takes up 6% (cc-pVTZ) and 12% (cc-pVQZ) of the total CD run time, is unaffected by the improvements of CD-WAC. For the total run, we attain a speed-up by a factor of 6.0 and 4.5. The difference in the speed-up between cc-pVTZ and cc-pVQZ is likely introduced by memory bottlenecks created by the inter-process communications involved in the computation and usage of the RI-V tensors  $O_p^{nm}$ . An indication for the latter is that the contribution of RI to the total CD run time is larger for cc-pVQZ than for cc-pVTZ. Nevertheless, the speed-ups are substantial. It should be emphasized that CD-WAC retains the high accuracy for larger systems with errors  $< 1$  m eV.

An additional benefit of the CD-WAC method is its ability to expedite the computation of the spectral function. The spectral function  $A(\omega)$  is derived from the imaginary part of the Green's function and its diagonal elements are given by  $A_{nn}(\omega) \propto \text{Im}[(\omega - \epsilon_n - \Sigma_n(\omega) + v_n^{xc})^{-1}]$ .<sup>37</sup> The spectral function provides the full spectral information, including access to the satellite spectrum. However, the computation of  $A(\omega)$  is burdensome with CD since it requires an evaluation of  $\Sigma_n^c$  for each frequency point  $\omega$ . If we have a frequency range of 50 eV and intervals of 0.01 eV, we compute the self-energy 5k times. In CD-WAC, we have an analytic approximation to the  $R_n$  term and only need to perform the numerical integration in Equation (20) with pre-computed matrix elements  $W_{nm}^c(i\omega)$ . Even for a small system, such as a single water molecule, CD-WAC reduces the computational cost for the computation of  $A(\omega)$  by at least three orders of magnitude compared to CD.

## 6 Conclusions

We have presented an efficient and scalable *GW* implementation for core-level calculations. Building on our previous work,<sup>22</sup> we use the highly accurate and numerically stable CD method to compute the *GW* self-energy for the full-frequency range on the real axis. In the present work, we have addressed the computational bottleneck of CD for deep core excitations by combining it with the AC of the *W* matrices, which is carried out using a modified version of Thiele's reciprocal differences' algorithm.

We have found that it is more difficult to enable the CD-WAC method for core than valence levels: i) We have devised an algorithm, which numerically stabilizes the Padé approximation for binding energies  $> 100$  eV. ii) While a set of imaginary frequency points is sufficient for valence states, real frequency points must be additionally included

in the AC of  $W$  when treating inner-shell excitations. We have implemented a heuristic procedure which places the additional real frequency in two different frequency regions, which are defined by the core and valence residues. Using the notation CD-WAC( $N_{\text{core}}$ ,  $N_{\text{valence}}$ ,  $N_{\text{Im}}$ ), we recommend CD-WAC(20,20,200) as safe default settings.

We have comprehensively benchmarked the CD-WAC approach against CD for 1s excitations. We have demonstrated that CD-WAC reproduces the essential features of the  $W$  and  $\Sigma$  matrix elements regardless of the type of the local basis set. We have studied the CORE65 benchmark set with  $G_0W_0$ @PBEh and partially self-consistent schemes, namely  $\text{ev}GW_0$ ,  $\text{ev}GW$  and  $G_{\Delta H}W_0$ , using PBE as starting point. For  $G_0W_0$ @PBEh, CD-WAC yields MAEs of 4 meV with respect to CD, independent on the basis set size. The error increases for the self-consistent schemes, but is with MAEs < 50 meV still excellent for  $\text{ev}GW$  and  $G_{\Delta H}W_0$ . In the  $\text{ev}GW_0$  case, the MAE is with 0.1 eV already in the range of the chemical C1s shifts. The reduction of the error is in principle possible. However, the CD-WAC approach is designed for large-scale calculations, for which we devised  $G_0W_0$ @PBEh<sup>47</sup> and more recently  $G_{\Delta H}W_0$ <sup>54</sup> methods as computationally affordable alternatives to  $\text{ev}GW_0$ .

The computational performance of CD-WAC has been demonstrated through numerical experiments. Compared to CD, the CD-WAC approach reduces the scaling for core-level  $GW$  calculations from  $O(N^5)$  to  $O(N^4)$  with respect to system size  $N$ . The prefactor introduced by computing the additional reference matrices for the AC of  $W$  is small, and the cross-over point between CD and CD-WAC is around 20 atoms. The speed-up has been assessed for a medium-sizes system of 116 atoms, for which we found that CD-WAC accelerates the total run time by at least a factor of 5 to 6.

The CD-WAC method represents a valuable contribution to the current efforts of reducing the scaling of  $GW$  calculations and paves the way for accurate computational predictions of core-level excitations in complex condensed matter systems. Further scaling reduction and the extension to periodic systems are part of ongoing and future work. Moreover, the CD-WAC dramatically speeds up the computation of the spectral function. The latter gives access to the satellite spectrum, which provides valuable complementary information to QP excitations.

**Acknowledgement** The authors acknowledge financial support by the Emmy Noether Programme of the German Research Foundation (project number 453275048) and thank the ZIH of the TU Dresden, the Jülich Supercomputer Computer Center and the Finnish CSC - IT Center for Science for providing computational resources.

## Supporting Information Available

The supplementary information is available free of charge. We include the tables comparing the CD and CD-WAC methods for different  $GW$  flavors (Tables S1 to S3). We also present the box plots of the CD-WAC absolute errors with respect to CD at the  $G_0W_0$ PBEh( $\alpha=0.45$ ) level of theory for increasing sizes of additional frequency points (Figure S1), and the self-energy matrix elements for the pyrrole molecule for both CD and CD-WAC at the  $G_{\Delta H}W_0$ @PBE level of theory (Figure S2).

## References

- (1) Siegbahn, K. *ESCA Applied to Free Molecules*; North-Holland Publishing: Amsterdam; London, 1969.
- (2) Bagus, P. S.; Ilton, E. S.; Nelin, C. J. The Interpretation of XPS Spectra: Insights into Materials Properties. *Surf. Sci. Rep.* **2013**, *68*, 273–304.
- (3) Van der Heide, P. *X-ray photoelectron spectroscopy: an introduction to principles and practices*; John Wiley & Sons, 2011.
- (4) Hohenberg, P.; Kohn, W. Inhomogeneous Electron Gas. *Phys. Rev.* **1964**, *136*, B864–B871.
- (5) Kohn, W.; Sham, L. J. Self-Consistent Equations Including Exchange and Correlation Effects. *Phys. Rev.* **1965**, *140*, A1133–A1138.
- (6) Bagus, P. S. Self-consistent-field wave functions for hole states of some Ne-like and Ar-like ions. *Phys. Rev.* **1965**, *139*, A619.
- (7) Susi, T.; Mowbray, D. J.; Ljungberg, M. P.; Ayala, P. Calculation of the graphene C 1s core level binding energy. *Phys. Rev. B* **2015**, *91*, 081401.
- (8) Susi, T.; Scardamaglia, M.; Mustonen, K.; Tripathi, M.; Mittelberger, A.; Al-Hada, M.; Amati, M.; Sezen, H.; Zeller, P.; Larsen, A. H.; Mangler, C.; Meyer, J. C.; Gregoratti, L.; Bittencourt, C.; Kotakoski, J. Intrinsic core level photoemission of suspended monolayer graphene. *Phys. Rev. Mater.* **2018**, *2*, 074005.
- (9) Pueyo Bellafont, N.; Álvarez Saiz, G.; Viñes, F.; Illas, F. Performance of Minnesota functionals on predicting core-level binding energies of molecules containing main-group elements. *Theor. Chem. Acc.* **2016**, *135*, 35.

(10) Pueyo Bellafont, N.; Viñes, F.; Illas, F. Performance of the TPSS Functional on Predicting Core Level Binding Energies of Main Group Elements Containing Molecules: A Good Choice for Molecules Adsorbed on Metal Surfaces. *J. Chem. Theory Comput.* **2016**, *12*, 324.

(11) Viñes, F.; Sousa, C.; Illas, F. On the prediction of core level binding energies in molecules, surfaces and solids. *Phys. Chem. Chem. Phys.* **2018**, *20*, 8403–8410.

(12) Aarva, A.; Deringer, V. L.; Sainio, S.; Laurila, T.; Caro, M. A. Understanding X-ray spectroscopy of carbonaceous materials by combining experiments, density functional theory and machine learning. Part I: fingerprint spectra. *Chem. Mater.* **2019**, *31*, 9243.

(13) Aarva, A.; Deringer, V. L.; Sainio, S.; Laurila, T.; Caro, M. A. Understanding X-ray spectroscopy of carbonaceous materials by combining experiments, density functional theory and machine learning. Part II: quantitative fitting of spectra. *Chem. Mater.* **2019**, *31*, 9256.

(14) Kahk, J. M.; Lischner, J. Accurate Absolute Core-Electron Binding Energies of Molecules, Solids, and Surfaces from First-Principles Calculations. *Phys. Rev. Mater.* **2019**, *3*, 100801.

(15) Hait, D.; Head-Gordon, M. Highly Accurate Prediction of Core Spectra of Molecules at Density Functional Theory Cost: Attaining Sub-electronvolt Error from a Restricted Open-Shell Kohn–Sham Approach. *J. Phys. Chem. Lett.* **2020**, *11*, 775–786, PMID: 31917579.

(16) Besley, N. A. Modeling of the spectroscopy of core electrons with density functional theory. *WIREs Comput. Mol. Sci.* **2021**, *11*, e1527.

(17) Kahk, J. M.; Michelitsch, G. S.; Maurer, R. J.; Reuter, K.; Lischner, J. Core Electron Binding Energies in Solids from Periodic All-Electron  $\Delta$ -Self-Consistent-Field Calculations. *J. Phys. Chem. Lett.* **2021**, *12*, 9353–9359.

(18) Klein, B. P.; Hall, S. J.; Maurer, R. J. The nuts and bolts of core-hole constrained ab initio simulation for K-shell x-ray photoemission and absorption spectra. *J. Phys.: Condens. Matter* **2021**, *33*, 154005.

(19) Kahk, J. M.; Lischner, J. Predicting core electron binding energies in elements of the first transition series using the  $\Delta$ -self-consistent-field method. *Faraday Discuss.* **2022**, *236*, 364–373.

(20) Kahk, J. M.; Lischner, J. Combining the  $\Delta$ -Self-Consistent-Field and GW Methods for Predicting Core Electron Binding Energies in Periodic Solids. *J. Chem. Theory Comput.* **2023**, *0*, null, PMID: 37163299.

(21) Pinheiro, M.; Caldas, M. J.; Rinke, P.; Blum, V.; Scheffler, M. Length dependence of ionization potentials of transacetylenes: Internally consistent DFT/GW approach. *Phys. Rev. B* **2015**, *92*, 195134.

(22) Golze, D.; Wilhelm, J.; Van Setten, M. J.; Rinke, P. Core-level binding energies from GW: An efficient full-frequency approach within a localized basis. *J. Chem. Theory Comput.* **2018**, *14*, 4856–4869.

(23) Michelitsch, G. S.; Reuter, K. Efficient Simulation of Near-Edge X-Ray Absorption Fine Structure (NEXAFS) in Density-Functional Theory: Comparison of Core-Level Constraining Approaches. *J. Chem. Phys.* **2019**, *150*, 074104.

(24) Golze, D.; Hirvensalo, M.; Hernández-León, P.; Aarva, A.; Etula, J.; Susi, T.; Rinke, P.; Laurila, T.; Caro, M. A. Accurate Computational Prediction of Core-Electron Binding Energies in Carbon-Based Materials: A Machine-Learning Model Combining Density-Functional Theory and GW. *Chem. Mater.* **2022**, *34*, 6240–6254.

(25) S. J. Hall, R. J. M., B. P. Klein Self-interaction error induces spurious charge transfer artefacts in core-level simulations of x-ray photoemission and absorption spectroscopy of metal-organic interfaces. *arXiv:2112.00876* **2020**,

(26) Stanton, J. F.; Bartlett, R. J. The equation of motion coupled-cluster method. A systematic biorthogonal approach to molecular excitation energies, transition probabilities, and excited state properties. *J. Chem. Phys.* **1993**, *98*, 7029–7039.

(27) Schirmer, J. Beyond the random-phase approximation: A new approximation scheme for the polarization propagator. *Phys. Rev. A* **1982**, *26*, 2395.

(28) Kuleff, A. I.; Cederbaum, L. S. Ultrafast correlation-driven electron dynamics. *J. Phys. B: Atomic, Molecular and Optical Physics* **2014**, *47*, 124002.

(29) Liu, J.; Matthews, D.; Coriani, S.; Cheng, L. Benchmark Calculations of K-Edge Ionization Energies for First-Row Elements Using Scalar-Relativistic Core–Valence-Separated Equation-of-Motion Coupled-Cluster Methods. *J. Chem. Theory Comput.* **2019**, *15*, 1642–1651.

(30) Vidal, M. L.; Pokhilko, P.; Krylov, A. I.; Coriani, S. Equation-of-Motion Coupled-Cluster Theory to Model L-Edge X-ray Absorption and Photoelectron Spectra. *J. Phys. Chem. Lett.* **2020**, *11*, 8314–8321.

(31) Ambroise, M. A.; Dreuw, A.; Jensen, F. Probing Basis Set Requirements for Calculating Core Ionization and Core Excitation Spectra Using Correlated Wave Function Methods. *J. Chem. Theory Comput.* **2021**, *17*, 2832–2842.

(32) Vila, F. D.; Kas, J. J.; Rehr, J. J.; Kowalski, K.; Peng, B. Equation-of-Motion Coupled-Cluster Cumulant Green's Function for Excited States and X-Ray Spectra. *Front. Chem.* **2021**, *9*.

(33) Norman, P.; Dreuw, A. Simulating X-ray spectroscopies and calculating core-excited states of molecules. *Chem. Rev.* **2018**, *118*, 7208–7248.

(34) Hedin, L. New Method for Calculating the One-Particle Green's Function with Application to the Electron-Gas Problem. *Phys. Rev.* **1965**, *139*, A796–A823.

(35) Aryasetiawan, F.; Gunnarsson, O. The GW method. *Rep. Prog. Phys.* **1998**, *61*, 237.

(36) Reining, L. The GW approximation: content, successes and limitations. *Wiley Interdiscip. Rev. Comput. Mol. Sci.* **2018**, *8*, e1344.

(37) Golze, D.; Dvorak, M.; Rinke, P. The GW compendium: A practical guide to theoretical photoemission spectroscopy. *Front. Chem.* **2019**, *7*, 377.

(38) Jacquemin, D.; Duchemin, I.; Blase, X. 0–0 energies using hybrid schemes: Benchmarks of TD-DFT, CIS (D), ADC (2), CC2, and BSE/GW formalisms for 80 real-life compounds. *J. Chem. Theory Comput.* **2015**, *11*, 5340–5359.

(39) Bintrim, S. J.; Berkelbach, T. C. Full-frequency GW without frequency. *J. Chem. Phys.* **2021**, *154*, 041101.

(40) Rasmussen, A.; Deilmann, T.; Thygesen, K. S. Towards Fully Automated GW Band Structure Calculations: What We Can Learn from 60.000 Self-Energy Evaluations. *npj Comput Mater* **2021**, *7*, 1–9.

(41) van Setten, M. J.; Caruso, F.; Sharifzadeh, S.; Ren, X.; Scheffler, M.; Liu, F.; Lischner, J.; Lin, L.; Deslippe, J. R.; Louie, S. G.; others GW100: Benchmarking  $G_0W_0$  for molecular systems. *J. Chem. Theory Comput.* **2015**, *11*, 5665–5687.

(42) Stuke, A.; Kunkel, C.; Golze, D.; Todorović, M.; Margraf, J. T.; Reuter, K.; Rinke, P.; Oberhofer, H. Atomic Structures and Orbital Energies of 61,489 Crystal-Forming Organic Molecules. *Sci Data* **2020**, *7*, 58.

(43) Bruneval, F.; Dattani, N.; van Setten, M. J. The GW Miracle in Many-Body Perturbation Theory for the Ionization Potential of Molecules. *Front. Chem.* **2021**, *9*.

(44) Aoki, T.; Ohno, K. Accurate quasiparticle calculation of x-ray photoelectron spectra of solids. *J. Phys. Condens. Matter* **2018**, *30*, 21LT01.

(45) van Setten, M. J.; Costa, R.; Vines, F.; Illas, F. Assessing GW approaches for predicting core level binding energies. *J. Chem. Theory Comput.* **2018**, *14*, 877–883.

(46) Voora, V. K.; Galhenage, R.; Hemminger, J. C.; Furche, F. Effective one-particle energies from generalized Kohn–Sham random phase approximation: A direct approach for computing and analyzing core ionization energies. *J. Chem. Phys.* **2019**, *151*, 134106.

(47) Golze, D.; Keller, L.; Rinke, P. Accurate absolute and relative core-level binding energies from GW. *J. Phys. Chem. Lett.* **2020**, *11*, 1840–1847.

(48) Keller, L.; Blum, V.; Rinke, P.; Golze, D. Relativistic correction scheme for core-level binding energies from GW. *J. Chem. Phys.* **2020**, *153*, 114110.

(49) Duchemin, I.; Blase, X. Robust analytic-continuation approach to many-body GW calculations. *J. Chem. Theory Comput.* **2020**, *16*, 1742–1756.

(50) Zhu, T.; Chan, G. K.-L. All-electron Gaussian-based  $G_0W_0$  for valence and core excitation energies of periodic systems. *J. Chem. Theory Comput.* **2021**, *17*, 727–741.

(51) Mejia-Rodriguez, D.; Kunitsa, A.; Aprà, E.; Govind, N. Scalable molecular GW calculations: Valence and core spectra. *J. Chem. Theory Comput.* **2021**, *17*, 7504–7517.

(52) Mejia-Rodriguez, D.; Kunitsa, A.; Aprà, E.; Govind, N. Basis Set Selection for Molecular Core-Level GW Calculations. *J. Chem. Theory Comput.* **2022**, *18*, 4919–4926.

(53) Li, J.; Chen, Z.; Yang, W. Renormalized Singles Green's Function in the T-Matrix Approximation for

Accurate Quasiparticle Energy Calculation. *J. Phys. Chem. Lett.* **2021**, *12*, 6203–6210, PMID: 34196553.

(54) Li, J.; Jin, Y.; Rinke, P.; Yang, W.; Golze, D. Benchmark of GW methods for core-level binding energies. *J. Chem. Theory Comput.* **2022**,

(55) Galleni, L.; Sajjadian, F. S.; Conard, T.; Escudero, D.; Pourtois, G.; van Setten, M. J. Modeling X-ray Photoelectron Spectroscopy of Macromolecules Using GW. *J. Phys. Chem. Lett.* **2022**, *13*, 8666–8672.

(56) Mukatayev, I.; Moevus, F.; Sklénard, B.; Olevano, V.; Li, J. XPS core-level chemical shift by ab initio many-body theory. *J. Phys. Chem. A* **2023**, *127*, 1642–1648.

(57) Yao, Y.; Golze, D.; Rinke, P.; Blum, V.; Kanai, Y. All-Electron BSE@GW Method for K-Edge Core Electron Excitation Energies. *J. Chem. Theory Comput.* **2022**,

(58) van Setten, M. J.; Weigend, F.; Evers, F. The GW-method for quantum chemistry applications: Theory and implementation. *J. Chem. Theory Comput.* **2013**, *9*, 232–246.

(59) Blase, X.; Attaccalite, C.; Olevano, V. First-principles GW calculations for fullerenes, porphyrins, phtalocyanine, and other molecules of interest for organic photovoltaic applications. *Phys. Rev. B* **2011**, *83*, 115103.

(60) Ren, X.; Rinke, P.; Blum, V.; Wieferink, J.; Tkatchenko, A.; Sanfilippo, A.; Reuter, K.; Scheffler, M. Resolution-of-identity approach to Hartree-Fock, hybrid density functionals, RPA, MP2 and GW with numeric atom-centered orbital basis functions. *New J. Phys.* **2012**, *14*, 053020.

(61) Deslippe, J.; Samsonidze, G.; Strubbe, D. A.; Jain, M.; Cohen, M. L.; Louie, S. G. BerkeleyGW: A massively parallel computer package for the calculation of the quasiparticle and optical properties of materials and nanostructures. *Comput. Phys. Commun.* **2012**, *183*, 1269–1289.

(62) Gonze, X.; Amadon, B.; Anglade, P.-M.; Beuken, J.-M.; Bottin, F.; Boulanger, P.; Bruneval, F.; Caliste, D.; Caracas, R.; Côté, M.; others ABINIT: First-principles approach to material and nanosystem properties. *Comput. Phys. Commun.* **2009**, *180*, 2582–2615.

(63) Klimeš, J.; Kaltak, M.; Kresse, G. Predictive GW calculations using plane waves and pseudopotentials. *Phys. Rev. B* **2014**, *90*, 075125.

(64) Hüser, F.; Olsen, T.; Thygesen, K. S. Quasiparticle GW calculations for solids, molecules, and two-dimensional materials. *Phys. Rev. B* **2013**, *87*, 235132.

(65) Wilhelm, J.; Del Ben, M.; Hutter, J. GW in the Gaussian and Plane Waves Scheme with Application to Linear Acenes. *J. Chem. Theory Comput.* **2016**, *12*, 3623–3635.

(66) Wilhelm, J.; Hutter, J. Periodic G W calculations in the Gaussian and plane-waves scheme. *Phys. Rev. B* **2017**, *95*, 235123.

(67) Ren, X.; Merz, F.; Jiang, H.; Yao, Y.; Rampp, M.; Lederer, H.; Blum, V.; Scheffler, M. All-Electron Periodic  $G_0W_0$  Implementation with Numerical Atomic Orbital Basis Functions: Algorithm and Benchmarks. *Phys. Rev. Mater.* **2021**, *5*, 013807.

(68) Rojas, H.; Godby, R. W.; Needs, R. Space-time method for ab initio calculations of self-energies and dielectric response functions of solids. *Phys. Rev. Lett.* **1995**, *74*, 1827.

(69) Liu, P.; Kaltak, M.; Klimeš, J.; Kresse, G. Cubic scaling G W: Towards fast quasiparticle calculations. *Phys. Rev. B* **2016**, *94*, 165109.

(70) Wilhelm, J.; Golze, D.; Talirz, L.; Hutter, J.; Pignedoli, C. A. Toward GW calculations on thousands of atoms. *J. Phys. Chem. Lett.* **2018**, *9*, 306–312.

(71) Wilhelm, J.; Seewald, P.; Golze, D. Low-scaling GW with benchmark accuracy and application to phosphorene nanosheets. *J. Chem. Theory Comput.* **2021**, *17*, 1662–1677.

(72) Duchemin, I.; Blase, X. Cubic-Scaling All-Electron GW Calculations with a Separable Density-Fitting Space-Time Approach. *J. Chem. Theory Comput.* **2021**, *17*, 2383–2393.

(73) Förster, A.; Visscher, L. Low-order scaling g 0 w 0 by pair atomic density fitting. *J. Chem. Theory Comput.* **2020**, *16*, 7381–7399.

(74) Förster, A.; Visscher, L. Low-Order Scaling Quasiparticle Self-Consistent GW for Molecules. *Front. Chem.* **2021**, *9*, 736591.

(75) Förster, A.; van Lenthe, E.; Spadotto, E.; Visscher, L. Two-component GW calculations: Cubic scaling implementation and comparison of partially self-consistent variants. *arXiv* **2023**, 2303.09979.

(76) Wright, J. N. S. J. *Numerical optimization*. 2006.

(77) Friedrich, C. Tetrahedron integration method for strongly varying functions: Application to the *GT* self-energy. *Phys. Rev. B* **2019**, *100*, 075142.

(78) Springer, M.; Aryasetiawan, F.; Karlsson, K. First-principles T-matrix theory with application to the 6 eV satellite in Ni. *Phys. Rev. Lett.* **1998**, *80*, 2389.

(79) Hedin, L. New method for calculating the one-particle Green's function with application to the electron-gas problem. *Phys. Rev.* **1965**, *139*, A796.

(80) Gross, E. K.; Runge, E. Many-particle theory. **1986**,

(81) Schirmer, J. *Many-body methods for atoms, molecules and clusters*; Springer, 2018.

(82) Adler, S. L. Quantum theory of the dielectric constant in real solids. *Phys. Rev.* **1962**, *126*, 413.

(83) Wiser, N. Dielectric constant with local field effects included. *Phys. Rev.* **1963**, *129*, 62.

(84) Hybertsen, M. S.; Louie, S. G. Electron correlation in semiconductors and insulators: Band gaps and quasi-particle energies. *Phys. Rev. B* **1986**, *34*, 5390.

(85) Vahtras, O.; Almlöf, J.; Feyereisen, M. Integral approximations for LCAO-SCF calculations. *Chem. Phys. Lett.* **1993**, *213*, 514–518.

(86) Godby, R. W.; Schlüter, M.; Sham, L. Self-energy operators and exchange-correlation potentials in semiconductors. *Phys. Rev. B* **1988**, *37*, 10159.

(87) Govoni, M.; Galli, G. Large scale GW calculations. *J. Chem. Theory Comput.* **2015**, *11*, 2680–2696.

(88) Yao, Y.; Golze, D.; Rinke, P.; Blum, V.; Kanai, Y. All-Electron BSE@ GW Method for K-Edge Core Electron Excitation Energies. *J. Chem. Theory Comput.* **2022**, *18*, 1569–1583.

(89) Nabok, D.; Tas, M.; Kusaka, S.; Durgun, E.; Friedrich, C.; Bihlmayer, G.; Blügel, S.; Hirahara, T.; Aguilera, I. Bulk and surface electronic structure of Bi 4 Te 3 from G W calculations and photoemission experiments. *Phys. Rev. Mater.* **2022**, *6*, 034204.

(90) George Jr, A.; others *Essentials of Padé approximants*; Elsevier, 1975.

(91) Vidberg, H.; Serene, J. Solving the Eliashberg equations by means of N-point Padé approximants. *Low Temp. Phys.* **1977**, *29*, 179–192.

(92) Chui, C.; Schempp, W.; Zeller, K.; Möller, H. M. Multivariate rational interpolation: Reconstruction of rational functions. *Multivariate Approximation Theory IV: Proceedings of the Conference at the Mathematical Research Institute at Oberwolfach, Black Forest, February 12–18, 1989*. 1989; pp 249–256.

(93) Milne-Thomson, L. M. *The calculus of finite differences*; American Mathematical Soc., 2000.

(94) Blum, V.; Gehrke, R.; Hanke, F.; Havu, P.; Havu, V.; Ren, X.; Reuter, K.; Scheffler, M. Ab initio molecular simulations with numeric atom-centered orbitals. *Comput. Phys. Commun.* **2009**, *180*, 2175–2196.

(95) Havu, V.; Blum, V.; Havu, P.; Scheffler, M. Efficient  $O(N)$  integration for all-electron electronic structure calculation using numeric basis functions. *J. Comput. Phys.* **2009**, *228*, 8367–8379.

(96) Zhang, I. Y.; Ren, X.; Rinke, P.; Blum, V.; Scheffler, M. Numeric atom-centered-orbital basis sets with valence-correlation consistency from H to Ar. *New J. Phys.* **2013**, *15*, 123033.

(97) Graves-Morris, P. Practical, reliable, rational interpolation. *IMA J. Appl. Math.* **1980**, *25*, 267–286.

(98) Celis, O. S. Numerical Continued Fraction Interpolation. *arXiv preprint arXiv:2109.10529* **2021**,

(99) Celis, O. S. Adaptive Thiele interpolation. *ACM Commun. Comput. Algebra* **2023**, *56*, 125–132.

(100) Choi, J.; Demmel, J.; Dhillon, I.; Dongarra, J.; Ostrouchov, S.; Petitet, A.; Stanley, K.; Walker, D.; Whaley, R. C. ScaLAPACK: A portable linear algebra library for distributed memory computers—Design issues and performance. *Comput. Phys. Commun.* **1996**, *97*, 1–15.

(101) Message Passing Interface Forum MPI: A Message-Passing Interface Standard Version 4.0. 2021.

(102) Perdew, J. P.; Burke, K.; Ernzerhof, M. Generalized gradient approximation made simple. *Phys. Rev. Lett.* **1996**, *77*, 3865.

(103) Atalla, V.; Yoon, M.; Caruso, F.; Rinke, P.; Scheffler, M. Hybrid density functional theory meets quasi-particle calculations: A consistent electronic structure approach. *Phys. Rev. B* **2013**, *88*, 165122.

(104) Dunning Jr, T. H. Gaussian basis sets for use in correlated molecular calculations. I. The atoms boron through neon and hydrogen. *J. Chem. Phys.* **1989**, *90*, 1007–1023.

(105) Wilson, A. K.; van Mourik, T.; Dunning Jr, T. H. Gaussian basis sets for use in correlated molecular calculations. VI. Sextuple zeta correlation consistent basis sets for boron through neon. *J. Mol. Struct.: THEOCHEM* **1996**, 388, 339–349.

(106) Weigend, F.; Ahlrichs, R. Balanced basis sets of split valence, triple zeta valence and quadruple zeta valence quality for H to Rn: Design and assessment of accuracy. *Phys. Chem. Chem. Phys.* **2005**, 7, 3297–3305.

(107) NOMAD Repository: FHI-aims calculations from CD-WAC method. <https://repository.nomad-coe.eu/datasets>, 2023; DOI to be added later.